

Naval Research Laboratory

Washington, DC 20375-5000



AD-A244 097



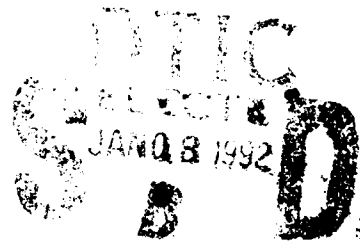
NRL Memorandum Report 6901

**Modeling Modal Transient Behavior of
GaAs Laser Diodes with Temperature
Dependent Rate Equations and
Comparison to Experimental Data**

WENDY L. LIPPINCOTT AND WILLIAM C. COLLINS

*Communication Systems Technology Branch
Space Systems Development Department*

December 26, 1991



92-00339



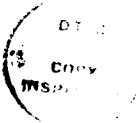
Approved for public release, distribution unlimited

REPORT DOCUMENTATION PAGE			Form Approved OMB No 0704-0188	
Public reporting burden for this collection of information is estimated to average 1 hour per response, including the time for reviewing instructions, searching existing data sources, gathering and maintaining the data needed, and completing and reviewing the collection of information. Send comments regarding this burden estimate or any other aspect of this collection of information, including suggestions for reducing this burden, to Washington Headquarters Services, Directorate for Information Operations and Reports, 1215 Jefferson Davis Highway, Suite 1204, Arlington, VA 22202-4302, and to the Office of Management and Budget, Paperwork Reduction Project (0704-0188), Washington, DC 20503.				
1. AGENCY USE ONLY (Leave blank)		2. REPORT DATE 1991 December 26	3. REPORT TYPE AND DATES COVERED	
4. TITLE AND SUBTITLE Modeling Modal Transient Behavior of GaAs Laser Diodes with Temperature Dependent Rate Equations			5. FUNDING NUMBERS SPAWAR-004-4/014-90	
6. AUTHOR(S) Wendy L. Lippincott and William C. Collins				
7. PERFORMING ORGANIZATION NAME(S) AND ADDRESS(ES) Naval Research Laboratory Washington, DC 20375-5000			8. PERFORMING ORGANIZATION REPORT NUMBER NRL Memorandum Report 6901	
9. SPONSORING/MONITORING AGENCY NAME(S) AND ADDRESS(ES) SPAWAR			10. SPONSORING/MONITORING AGENCY REPORT NUMBER SPAWAR-004-5/014-90	
11. SUPPLEMENTARY NOTES				
12a. DISTRIBUTION/AVAILABILITY STATEMENT Approved for public release; distribution unlimited.			12b. DISTRIBUTION CODE	
13. ABSTRACT (Maximum 200 words) Theoretical predictions based on temperature dependent rate equations are made of the pulse response of the individual axial modes of high power laser diodes. The temperature transients in the active area of the lasers are simulated with a finite element code and entered into the rate equations which describe the time evolution of both the carrier population and the photon number inside the laser cavity. Experimentally, the laser diodes are triggered by a fast electrical pulse and the modes of gain-guided AlGaAs laser diodes are dispersed with an echelle grating and individually imaged onto a scanning avalanche photodiode (APD). The results of this study showed that modal instabilities during pulsed operation of the laser diodes can be separated into two types of transients: mode buildup transients and thermally-induced transients. Mode buildup transients, due to feedback from the cavity gradually causing power to concentrate in a few modes, were found to last up to 60 ns depending on laser length, whereas thermally-induced transients were found to last several hundred nanoseconds and are dependent on the overall efficiency of the laser. Our experimental results show that broad-stripe lasers, which minimize current spreading, have much smaller temperature transients as compared to narrow single-stripe lasers.				
14. SUBJECT TERMS			15. NUMBER OF PAGES 99	
			16. PRICE CODE	
17. SECURITY CLASSIFICATION OF REPORT UNCLASSIFIED	18. SECURITY CLASSIFICATION OF THIS PAGE UNCLASSIFIED	19. SECURITY CLASSIFICATION OF ABSTRACT UNCLASSIFIED	20. LIMITATION OF ABSTRACT SAR	

TABLE OF CONTENTS

SECTION	PAGE
Chapter 1. Introduction	1
Chapter 2. Experimental Measurements Characterizing the Pulse Response of Laser Diodes	3
2.1 Determination of the pulse response of the modes of the laser diodes with an APD	3
2.2 General discussion of experimental results obtained using the APD	20
2.3 Determination of the relaxation oscillation frequencies of the laser diodes with a streak camera	21
Chapter 3. Thermal Modeling with the NASTRAN Finite Element Code	26
3.1 Setting up the NASTRAN finite element code	26
3.2 Determination of heat sources within the diode	30
3.3 Steady-state results	34
3.4 Transient results and discussion	34
3.5 Effect of varying cell sizes	37
Chapter 4. Temperature-Dependent Rate Equations Model	38
4.1 Introduction	38
4.2 Description of the rate equations	38
4.3 Determination of the stimulated emission factor and the transparency electron current density	44
4.4 Line shape factor and the gain spectral linewidth	51
4.5 Characterization of the spontaneous emission factor	51
4.6 Incorporation of temperature effects	52
4.7 Refractive indexes	55
4.8 Confinement factor	55

4.9 Cavity loss coefficient	59
4.10 Spontaneous electron lifetime	60
4.11 Limitations of the rate equation model	62
Chapter 5. Using the Rate Equation Model	63
5.1 Introduction	63
5.2 Modeling the laser diodes without incorporating thermal effects	63
5.3 Modeling the laser diodes with thermal effects	73
5.4 General discussion of rate equation modeling results	76
Chapter 6. Conclusions	80
References	83
Appendix A. Computer Program Listing	88



Accession For	
NTIS GSA&I	<input checked="" type="checkbox"/>
DTIC TAB	<input type="checkbox"/>
Unannounced	<input type="checkbox"/>
Justification	
By	
Distribution/	
Availability Codes	
Dist	Avail and/or Special
A-1	

MODELING MODAL TRANSIENT BEHAVIOR OF GaAs LASER DIODES WITH TEMPERATURE DEPENDENT RATE EQUATIONS AND COMPARISON TO EXPERIMENTAL DATA

CHAPTER 1 INTRODUCTION

Recent advances in GaAlAs laser diodes have led to the development of low cost, long-lived, high power devices which have found application as transmitters in various communication systems.¹ One problem with the use of gain-guided laser diodes in communication systems, however, arises because significant power sharing between the axial lasing modes can occur over a period of order 100 ns when the lasers are pulsed. These modal "instabilities" (known as mode partition noise) can cause distortions in an optical communication system if the receiver samples only part of a dispersed optical beam. The power in the different axial modes will shift with time during the pulse, and so will the received signal if only selective modes are sampled.

This problem was investigated by first taking experimental data on several types of laser diode structures to quantify the magnitude of the modal instabilities. The modes are dispersed with an echelle grating and examined individually with an avalanche photodiode (APD) under various modulation conditions. The data was then compared to predictions of the modal instabilities made by solving temperature-dependent rate equations. The thermal impedance of the laser diodes and the temperature changes in the active area during a current pulse were modeled with a finite element code. A

detailed analysis of the laser was done 2-dimensionally, with a 3-dimensional analysis performed to determine the thermal impedance of the heat sink. The thermal properties were then entered into a program which numerically solves the rate equations of the diodes so that the power from the individual modes of the diode are determined as a function of time into the current pulse.

Broad-stripe, narrow-stripe and 10-stripe laser diodes were examined in this thesis. The broad-stripe and 10-stripe laser diodes are high power lasers, producing 200 to 600 mW of power. The 10-stripe laser diode array, consisting of 10 narrow stripe lasers spaced close together on the same chip, is an attempt to retain the high power of the broad stripe laser while reducing filamenting, a condition where lasing does not occur evenly throughout the gain area but tends to concentrate in certain areas called filaments. The narrow-stripe lasers are lower power but were also examined in this report, mainly as a comparison to the other structures and to help better understand laser diode behavior in general.

This report is organized with the experimental data described first. Then details are given on the finite element thermal modeling. The rate equation model is then described, and the lasers are modeled with the rate equation model first without and then with thermal effects. Finally a comparison is made of the experimental and calculated results, and suggestions are made for optimum laser designs that will minimize the modal instabilities of the laser diodes during modulation.

CHAPTER 2

EXPERIMENTAL MEASUREMENTS CHARACTERIZING THE PULSE RESPONSE OF LASER DIODES

2.1 Determination of the pulse response of the modes of the laser diodes with an APD

The pulse response of several laser diodes were examined with an APD. Figure 2.1 shows the experimental set-up used. The laser diode output is focused onto a slit at the spectrometer entrance. The incident beam then illuminates an echelle grating. The grating separates the laser modes which can be either imaged with a CCD camera or projected onto a scanning APD. The APD output is amplified and then sent to a Boxcar integrator which averages the data over a desired time period.

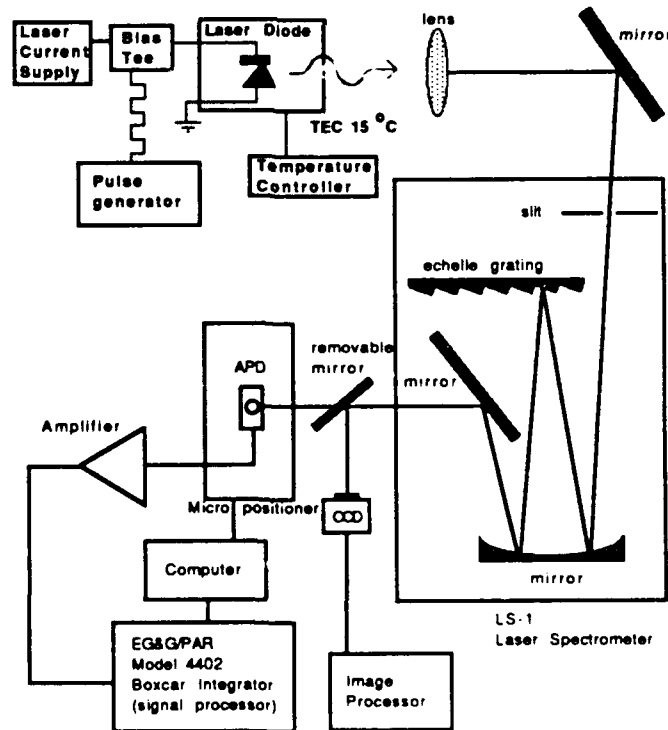


FIGURE 2.1 Experimental setup used to measure laser diode pulse response.

Several types of lasers were examined in this report. Table 2.1 lists the various lasers along with their pertinent characteristics.

TABLE 2.1

Lasers Tested Experimentally

Designation	Structure	Type	Width μm	Length μm	Threshold mA
SQW-5-300	SQW	narrow stripe	5	300	75
SQW-60-300	SQW	broad stripe	60	300	97
SQW-5-600	SQW	narrow stripe	5	600	130
SQW-60-600	SQW	broad stripe	60	600	102
MQW-4-250	MQW	narrow stripe	4	250	50
MQW-100-250	MQW	10-stripe	100	250	221

The first four lasers in Table 2.1 are AlGaAs graded-index separate-confinement heterostructure (GRINSCH) single-quantum-well (SQW) lasers mounted p-side-down from McDonnell Douglas Electronics Systems Company.^{2,3} These lasers are gain-guided in the lateral dimension. The 10-stripe multi-quantum-well (MQW) laser is from Spectra Diode Labs (SDL) and has 4 μm stripes on 10 μm centers.⁴ The narrow stripe MQW laser is also from SDL and has a 4 μm wide stripe. Figures 2.2 and 2.3 show the 10-stripe laser diode array and the broad stripe laser diode structures. The wavelengths are all near 820 nm.

Figure 2.4 shows the output waveforms for twelve dominant modes of the SQW-60-300 laser modulated at 105+100 mA with an 80 ns pulse with a 50% duty cycle. At this modulation depth the laser produces 80 mW of light. For the broad stripe lasers another cylindrical lens was used to focus the broad stripe onto the detector.

Two types of phenomena cause modal instabilities in pulsed laser diodes: mode buildup transients and thermal transients. Mode buildup transients occur over a relatively short period of time (10-60 ns) that depends on the

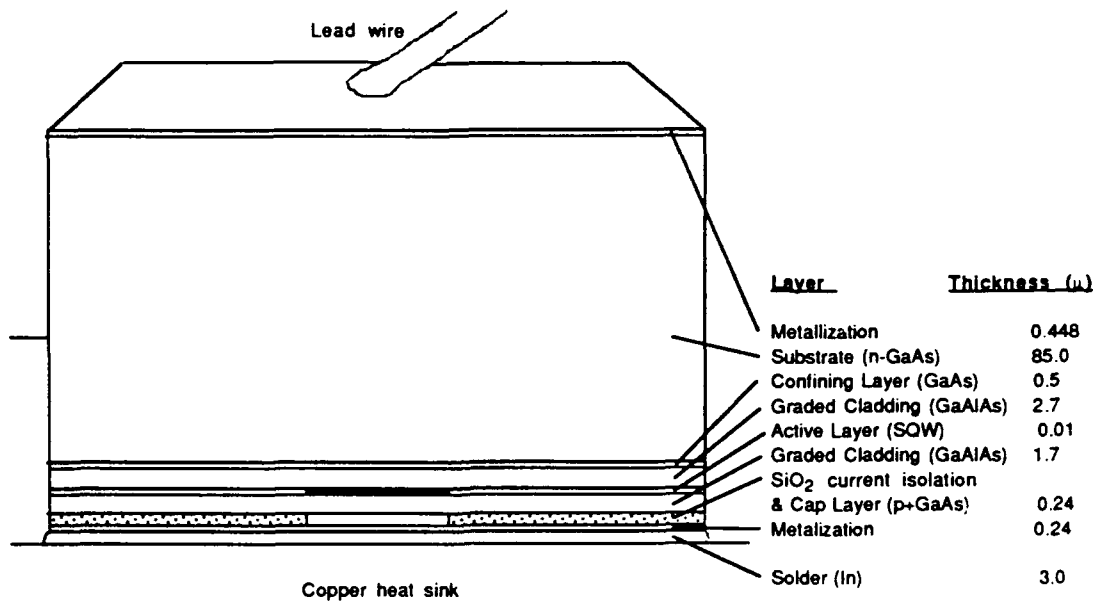


FIGURE 2.2 Broad-stripe GRINSCH SOW laser diode.

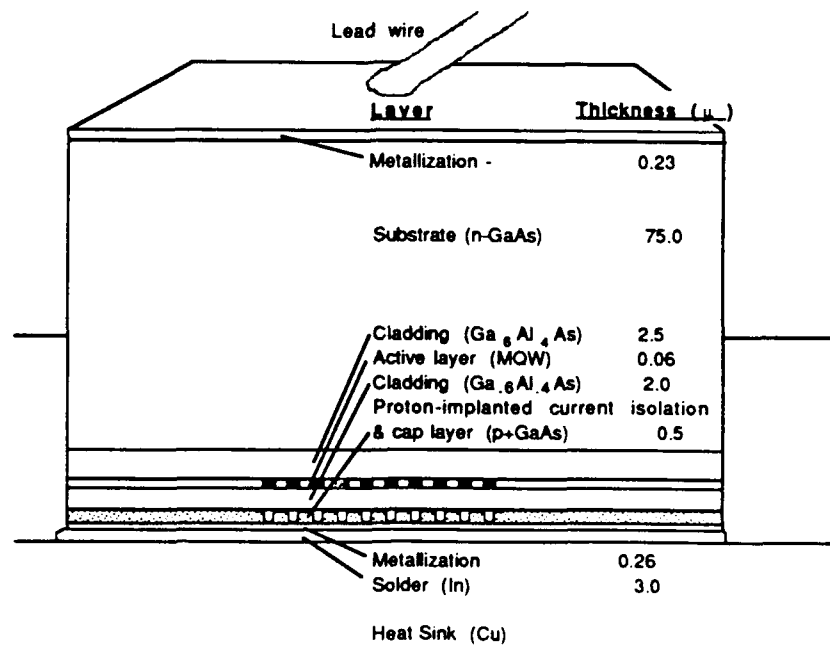


FIGURE 2.3 10-stripe MQW laser diode array.

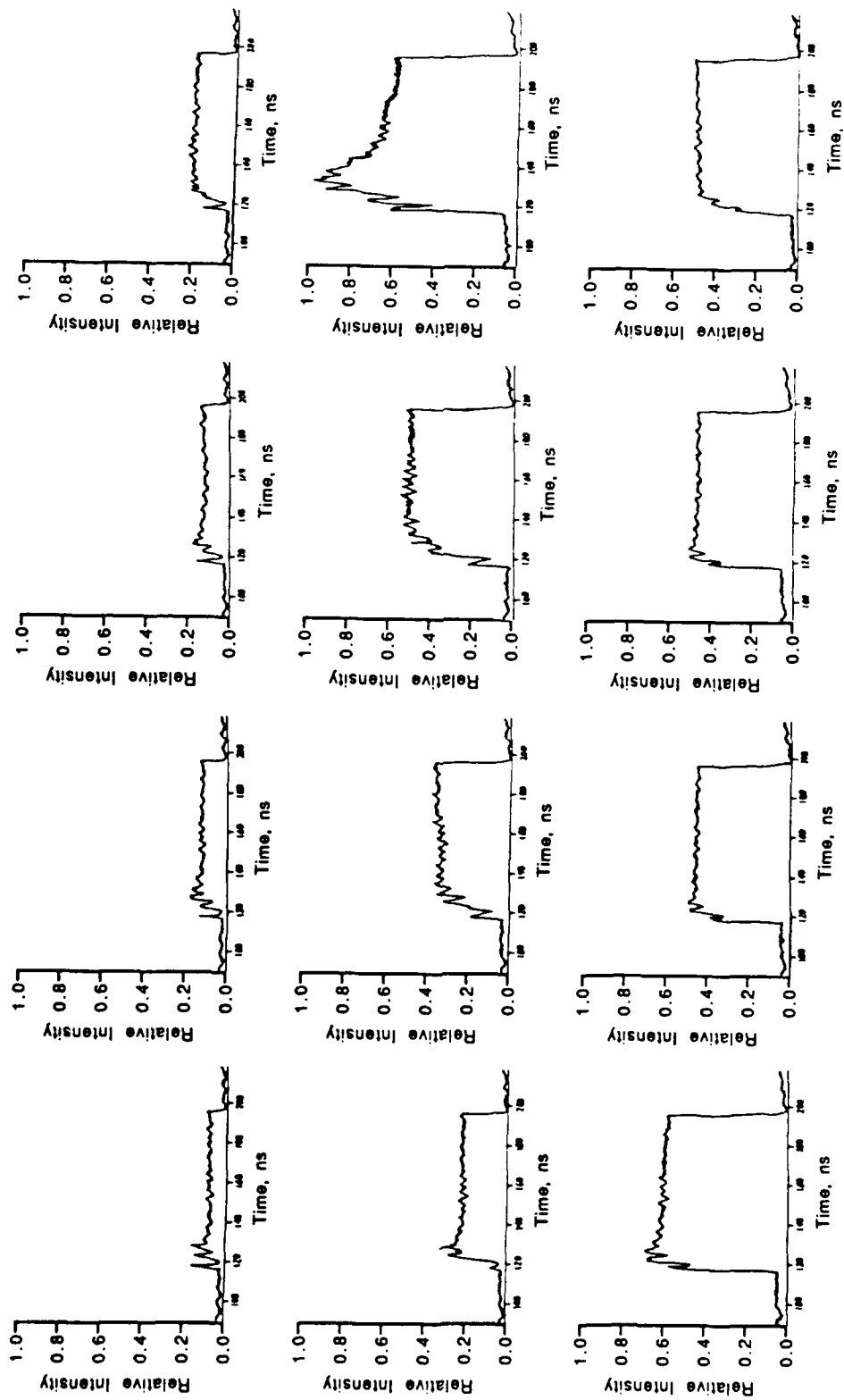


FIGURE 2.4 Output waveforms for twelve dominant modes of the SQW-60-300 laser modulated at 105+100 mA with an 80 ns pulse.

laser length. When the laser is first pulsed from threshold, many axial modes are excited because there are only slight differences in the gain factor for the different modes and the photon population in each of the modes (which drives the stimulated emission rate) is due initially to spontaneous emission.⁵ But after a while, the slight differences in the gain factor cause greater and greater differences in photon populations between the modes because a larger photon population will cause a larger stimulated emission rate for that particular mode. In other words, feedback gradually induces most of the power to concentrate in a few central modes even when there are only slight differences in their gain factors. This process takes approximately 10-60 ns depending on the photon lifetime in the cavity (which is related to the laser length). Thermal transients have much longer time constants (several hundred nanoseconds) and so the modal instabilities caused from these can last several microseconds. It should be noted that the severity of both the mode buildup transients and the thermal transients is directly related to the modulation depth of the pulse. Figure 2.4 shows that for the SQW-60-300 laser, large mode buildup-time transients occur over the first 10-20 ns into the pulse and then the pulse stabilizes out to a fairly flat waveform. Figure 2.5 shows a laser pulse with approximately the same modulation currents as for Figure 2.4 extended out to 1000 ns. As can be seen, the modes maintain fairly flat waveforms out to 1000 ns, indicating negligible thermal transients. A rough picture of the gain spectrum for the SQW-60-300 laser can be derived by taking the amplitude of each of the modes in Figure 2.5 at a specific point in time during the pulse and plotting these points against the frequency spacing between the modes. (For this laser the modes are spaced approximately 0.3 nm apart in wavelength.) It can be seen from Figure 2.5 that the gain spectrum for the SQW-60-300 laser for these particular operating conditions is not a

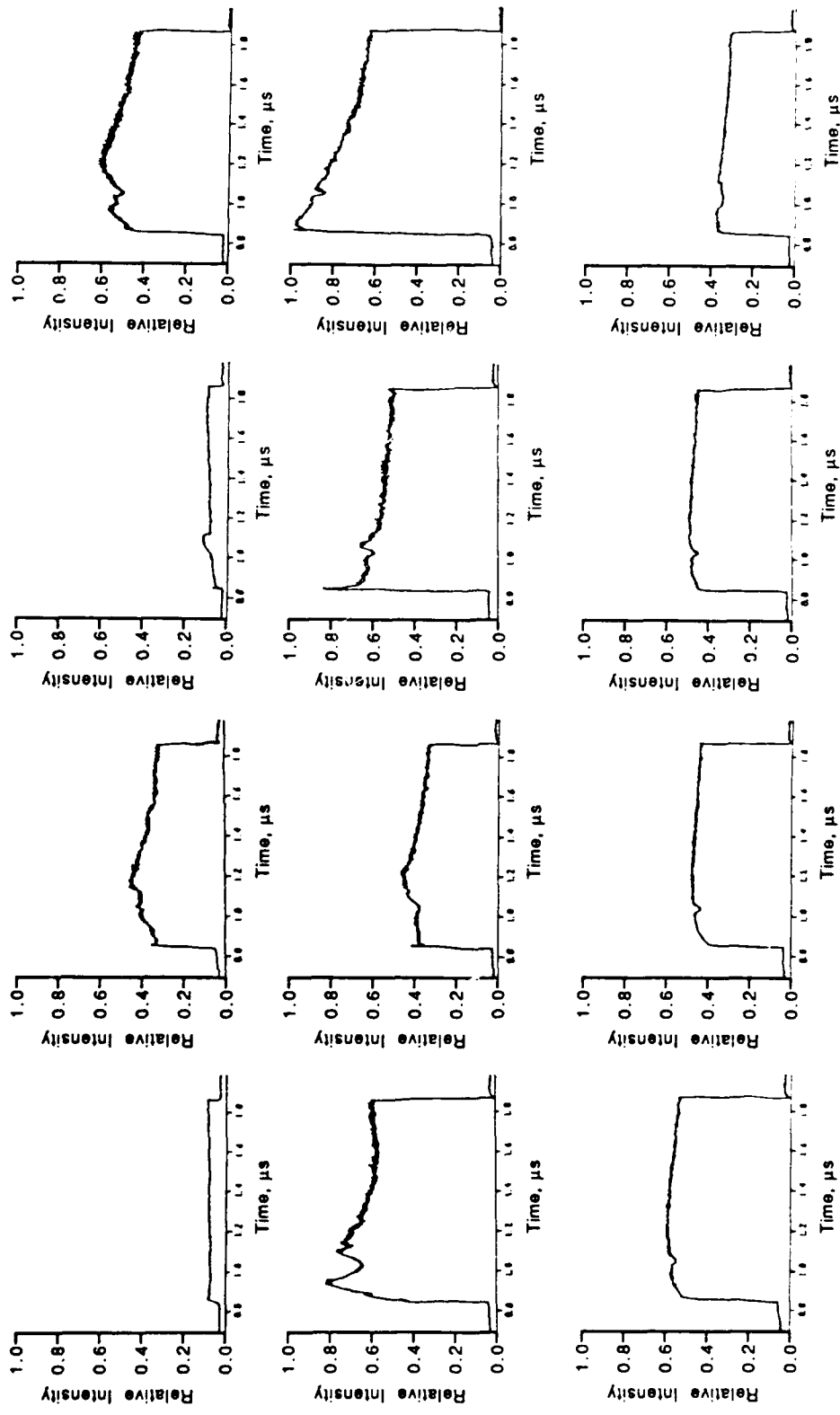


FIGURE 2.5 Output waveforms for twelve dominant modes of the SQW-60-300 laser modulated at 108+100 mA with a 1000 ns pulse.

smooth Lorentzian shaped curve but has a few ripples. This is probably due to competition between modes causing some of the modes to dominate over others. The modes of the 80 ns pulses do not correspond to the modes of the 1000 ns and 1600 ns pulses for the same lasers in Figures 2.4 through 2.11. This is because for the longer pulses the temperature in the active region at the start of the pulse will be different from that for the 80 ns pulse because for the longer pulse the temperature has more time to drop between pulses.

Figures 2.6 and 2.7 show the output waveforms for the ten dominant modes of the SQW-60-600 laser modulated at a 50% duty cycle from near threshold to 100 mA above threshold (and producing 65 mW of light). Figure 2.6 shows the waveforms up to 80 ns and Figure 2.7 up to 1000 ns. For this long 600 μm length laser, it is seen that the mode buildup-time transients last over 60 ns, but then the modes stabilize and remain fairly flat up to 1000 ns.

Modal instabilities for the SQW-5-300 are shown in Figures 2.8 and 2.9 for 80 ns and 1000 ns. This narrow stripe laser was modulated at 76+52 mA at a 50% duty cycle, producing 42 mW of light. At this modulation depth, this laser demonstrates both mode buildup transients and thermally-induced transients. The mode buildup-time transients are more severe and last 10-20 ns, whereas the thermally-induced transients cause gradual changes in the mode powers which last over 1000 ns. Figure 2.8 shows that the shorter wavelength modes (beginning at the upper left) lose power during the pulse and the longer wavelength modes gain power during the pulse. From this figure the peak of the gain curve is seen to shift through the modes as time progresses and the laser heats up due to the increased current.

The ten-stripe laser (MQW-100-250) output can be separated into several modes for each of the ten stripes. Figure 2.10 shows six dominant modes shown

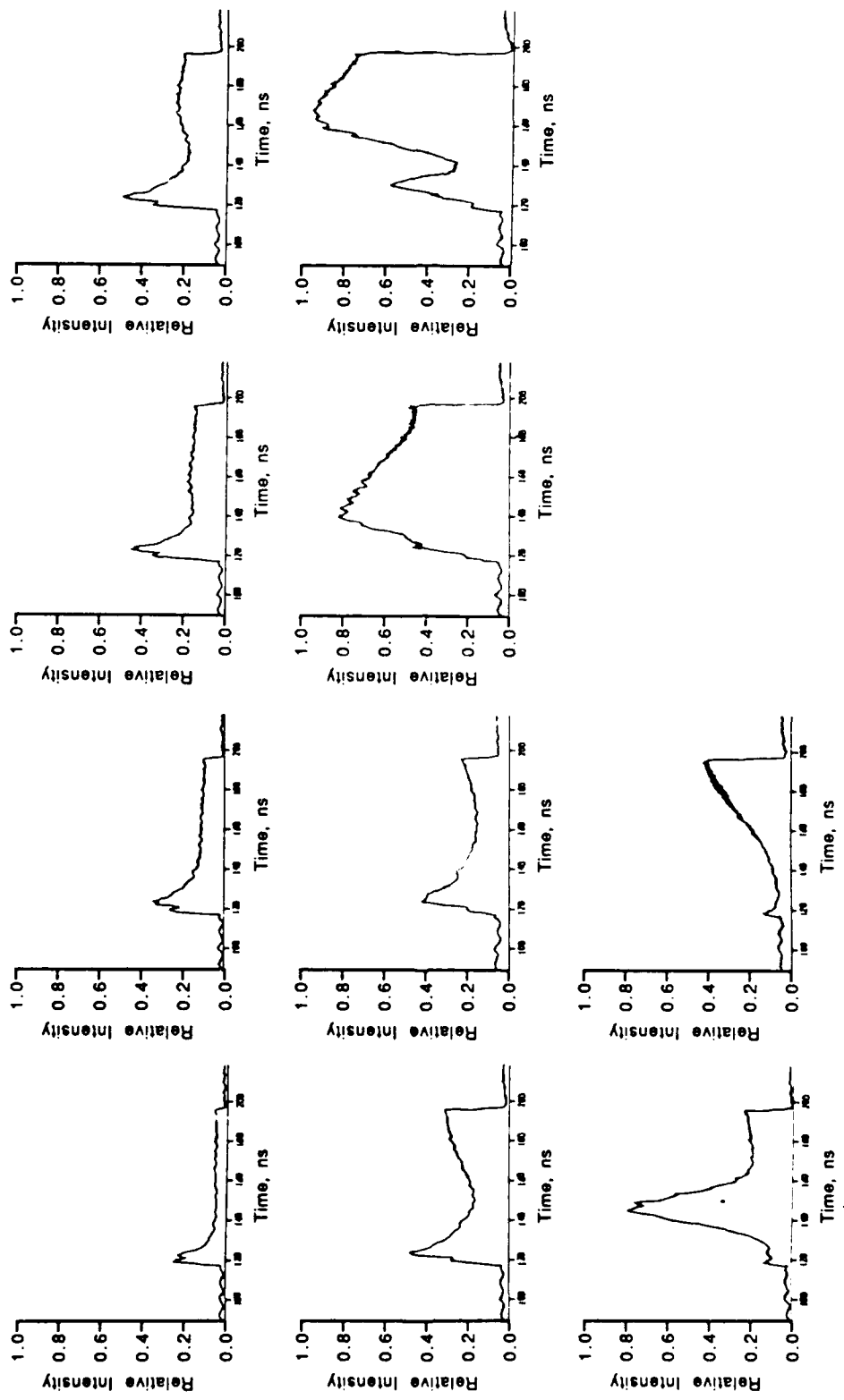


FIGURE 2.6 Output waveforms for ten dominant modes of the SQW-60-600 laser modulated at 105+100 mA with an 80 ns pulse.

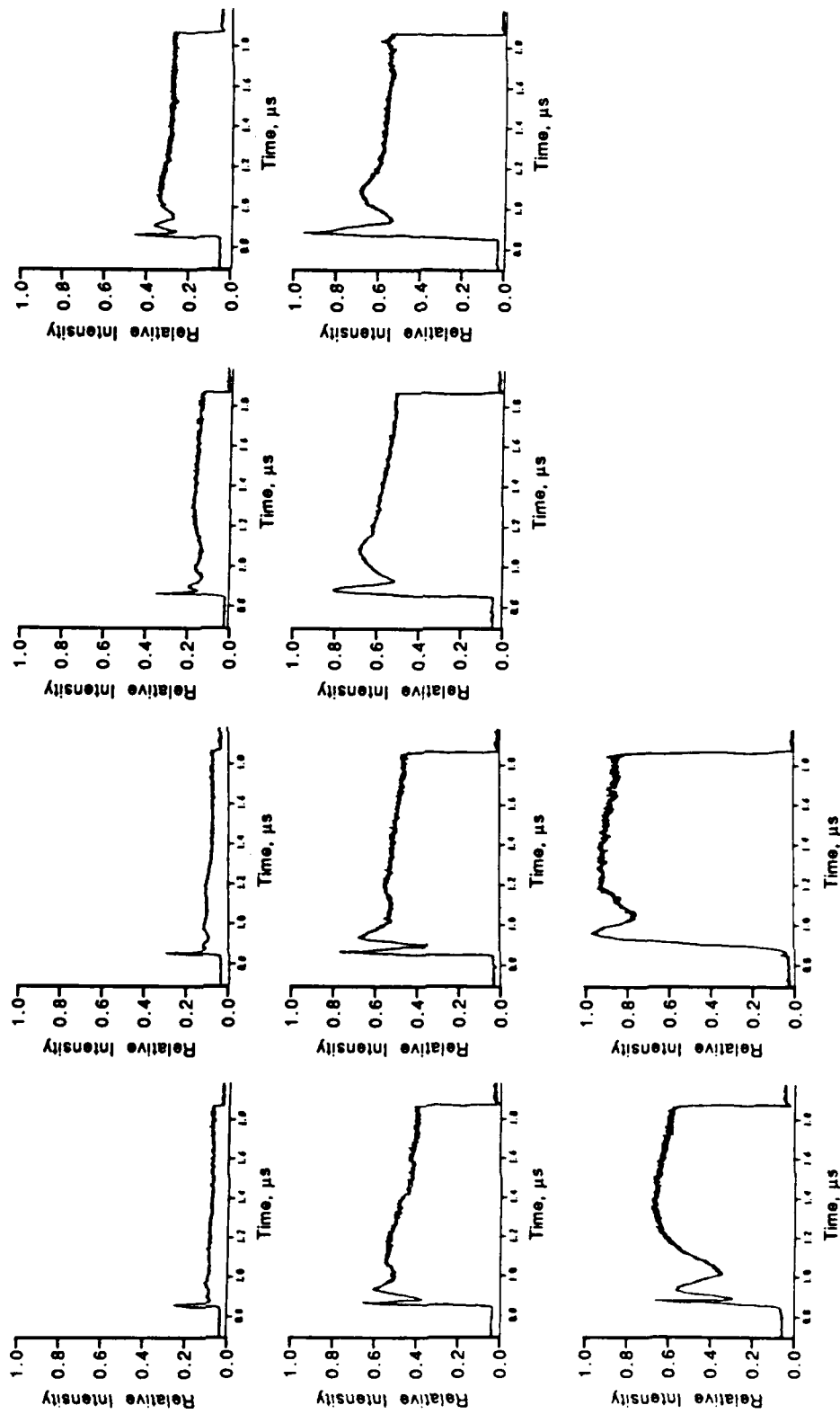


FIGURE 2.7 Output waveforms for ten dominant modes of the SQW-60-600 laser modulated at 101+100 mA with a 1000 ns pulse.

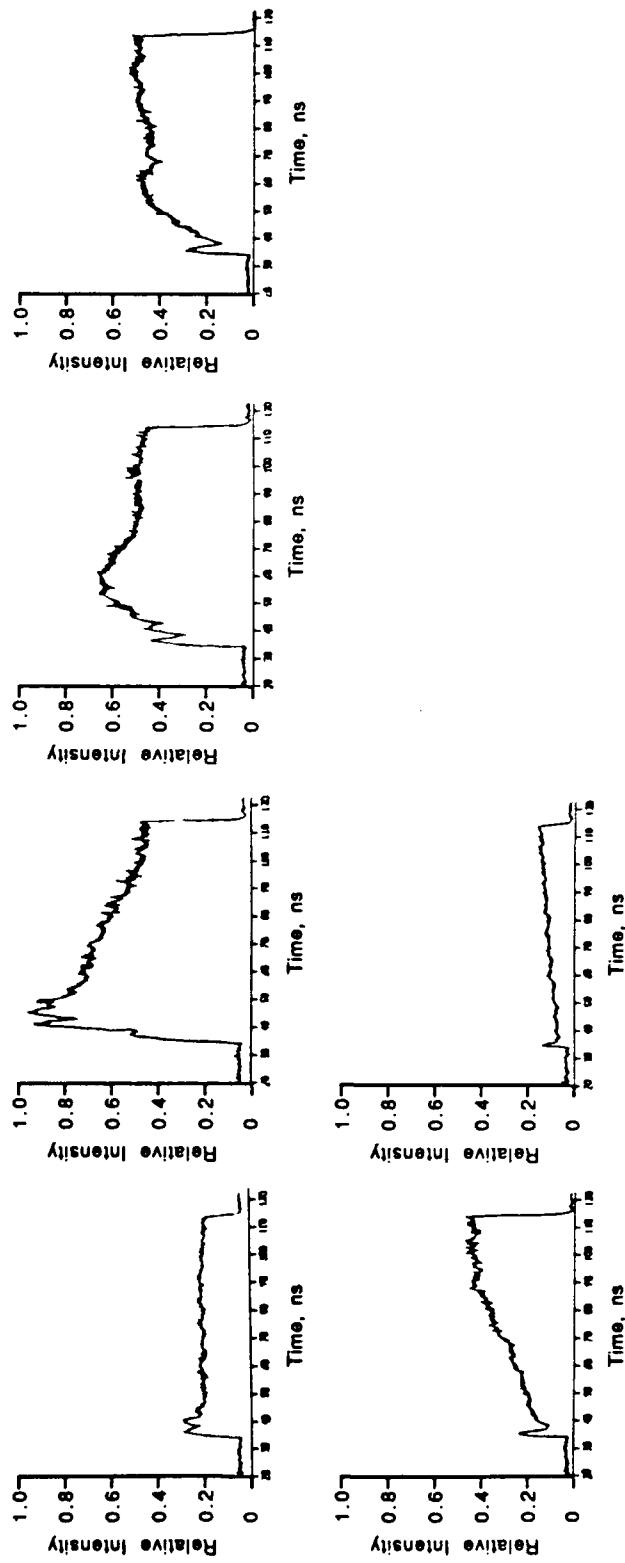


FIGURE 2.8 Output waveforms for six dominant modes of the SQW-5-300 laser modulated at 76+52 mA with an 80 ns pulse.

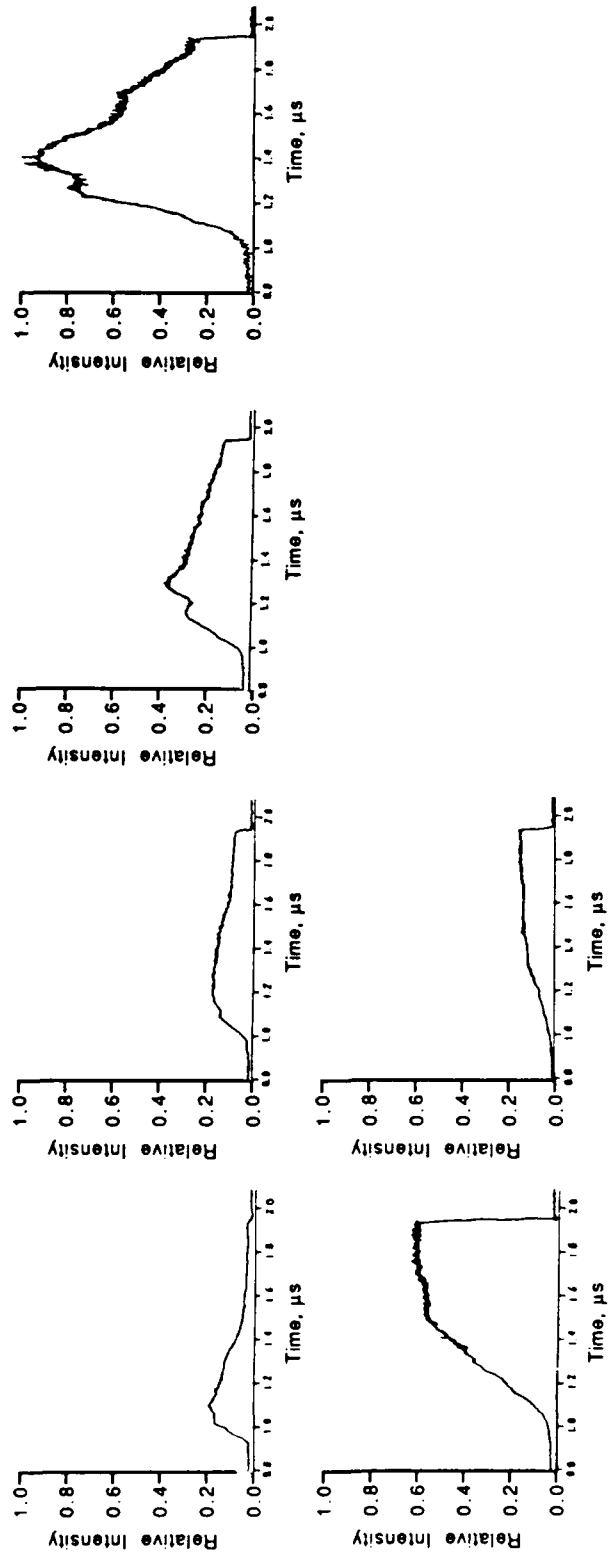


FIGURE 2.9 Output waveforms for six dominant modes of the SQW-5-300 laser modulated at 76+52 mA with a 1000 ns pulse.

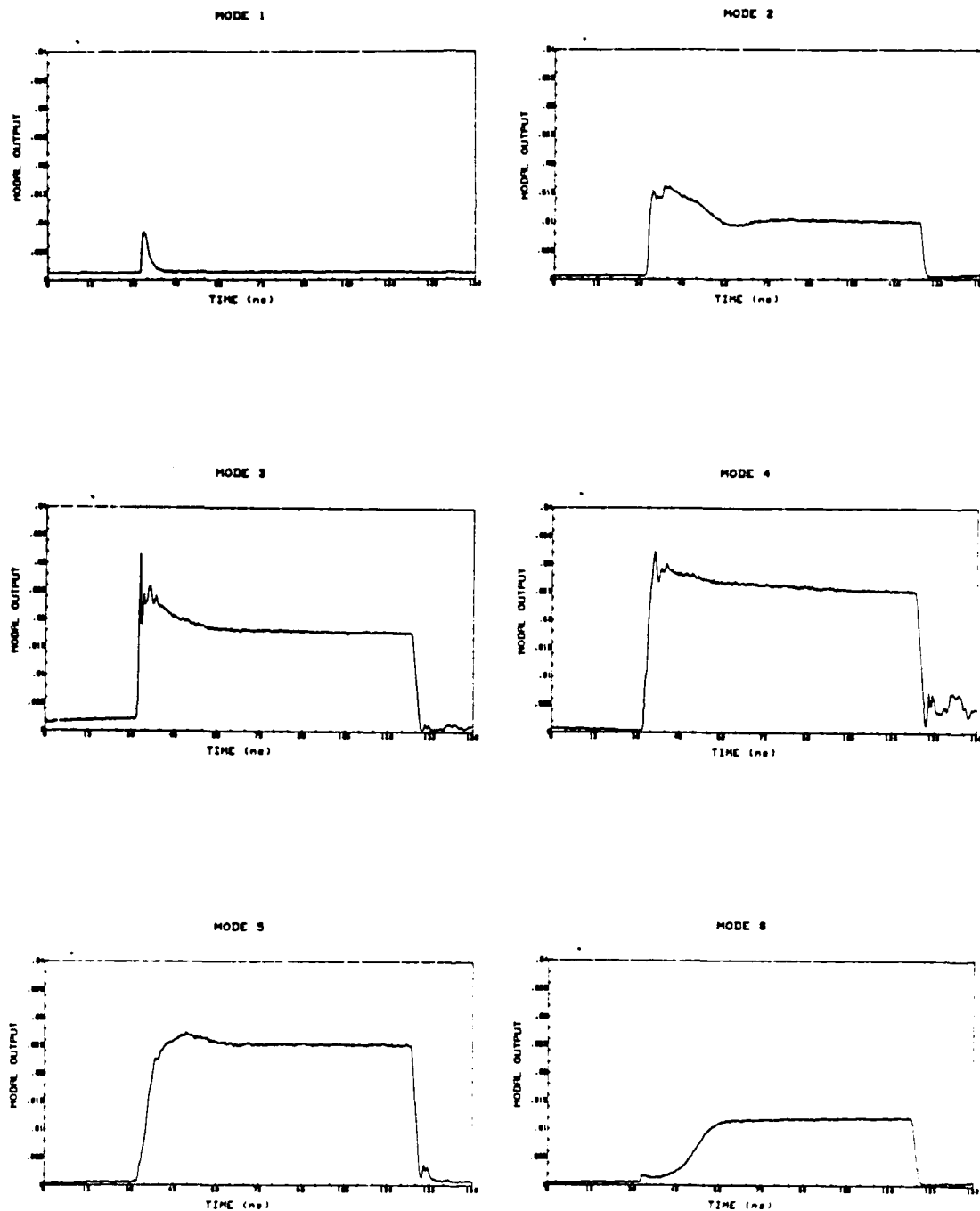


FIGURE 2.10 Output waveforms for six dominant modes of the 10-stripe laser diode array modulated at $200 + 130$ mA.

with the output from all the stripes combined for each mode. The pulse length is 100 ns with a 50% duty cycle. The modulation is 200 + 130 mA, with a peak optical power of 90 mW.

The narrow-stripe MQW laser (MQW-4-250) modal transients are shown over a periods of 80 ns and 1.6 μ s in Figures 2.11 and 2.12. The modulation current at a 50% duty cycle is 60+32 mA for a peak output power of 20 mW. The thermal transients for this laser are particularly severe causing modes to completely appear and disappear over a period of a few hundred nanoseconds.

Temperature changes in the active region causes the positions of the modes to shift as well as the relative intensity of the modes to shift. These two phenomena are respectively known as mode chirping and mode hopping. In the case of mode chirping, the actual wavelength of the individual modes shifts. In the case of mode hopping, the gain curve shifts causing the relative intensity of the modes to change. The emission wavelength for a typical GaAlAs laser will shift an average of 3 $\text{\AA}/^\circ\text{C}$.^{4,6} This is partly due to mode hopping and partly due to mode chirping. Mode hopping is the dominant effect, however mode chirping was measured to be 0.6 $\text{\AA}/^\circ\text{C}$ by Thompson⁶ and 0.93 $\text{\AA}/^\circ\text{C}$ by Dagenais, et al.,⁷ for AlGaAs lasers. In our lab we measured 2.5 $\text{\AA}/^\circ\text{C}$ and 0.6 $\text{\AA}/^\circ\text{C}$ for the total modal shift and for mode chirping for the SQW-60-300 laser. For the lasers with large thermally-induced transients, mode chirping can be severe enough to cause the mode to move across the detector area during the pulse duration. For the experimental data in this report, the corresponding detector diameter in wavelength units was 0.4 \AA and was dependent on the size of the detector. The modes had roughly a Gaussian shape with a FWHM of $\sim 1 \text{\AA}$. If the thermal shift is greater than $\sim 0.5 \text{ }^\circ\text{C}$ then the detector will shift through the longitudinal mode during the pulse, and therefore the data will not accurately measure the degree of mode

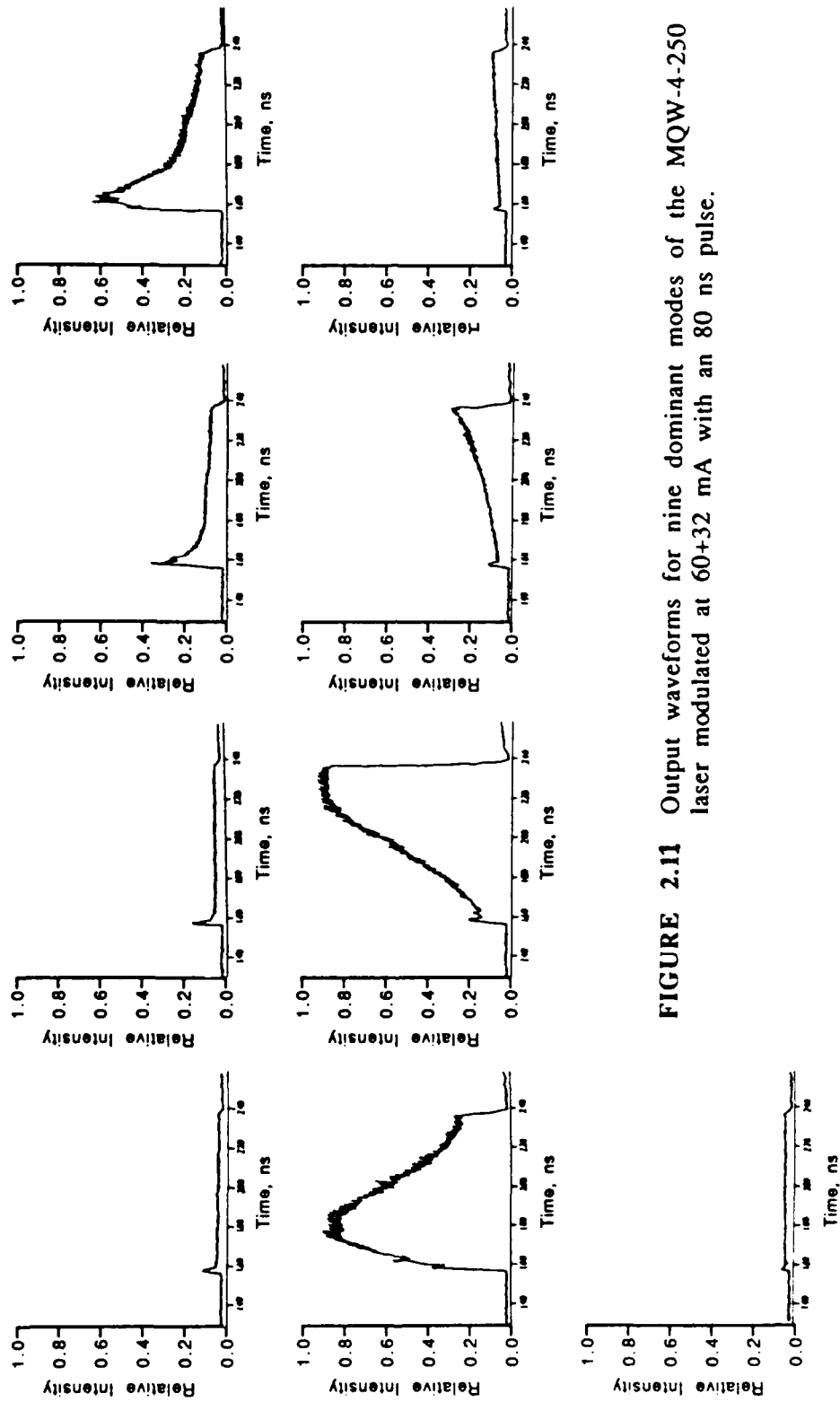


FIGURE 2.11 Output waveforms for nine dominant modes of the MQW-4-250 laser modulated at 60+32 mA with an 80 ns pulse.

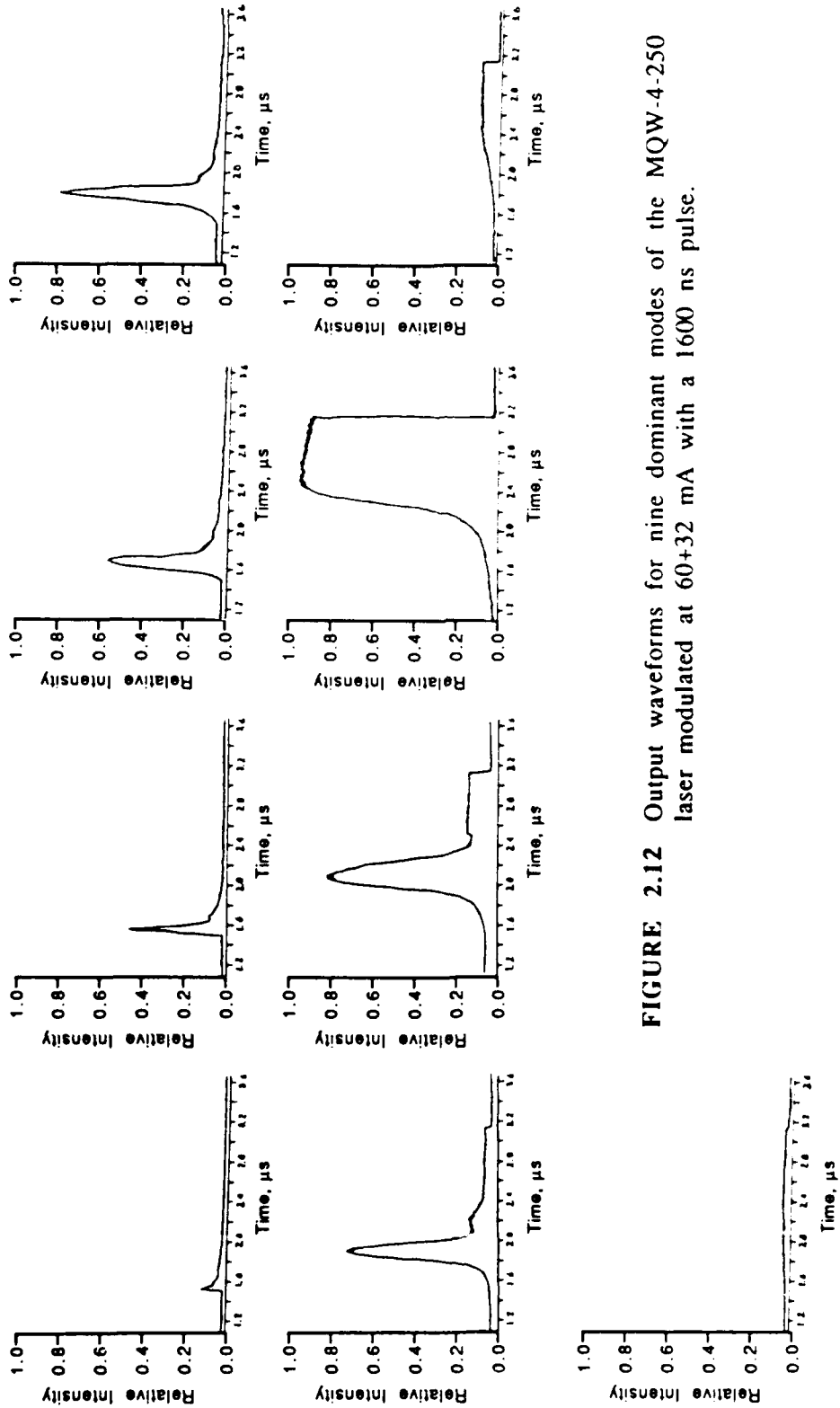


FIGURE 2.12 Output waveforms for nine dominant modes of the MQW-4-250 laser modulated at 60+32 mA with a 1600 ns pulse.

hopping. For the MQW-4-250 and the SQW-5-300 lasers at the long pulse lengths this is the case. However, the data for the shorter 80 ns excitation pulses are still representative of the degree of mode hopping.

One way to measure the severity of the modal transients in a 10-stripe laser is to measure the average standard deviation of the ten intensity waveforms for each of the dominant modes from a square wave when the laser is electrically driven by a square current pulse above the bias current. This was done for the 10-stripe laser at a constant modulation depth of 130 mA by varying the bias current around the threshold value of 200 mA. Figure 2.13 shows the results plotted. At a bias of 190 mA, slightly below threshold, there is a standard deviation of 0.10 whereas at 210 mA, slightly above threshold, there is a standard deviation of 0.17. These are large differences in the severity of the modal transients. These kind of fluctuations are also apparent when the modulation depth is changed. In general, the modal transients are less severe with lower modulation depth.

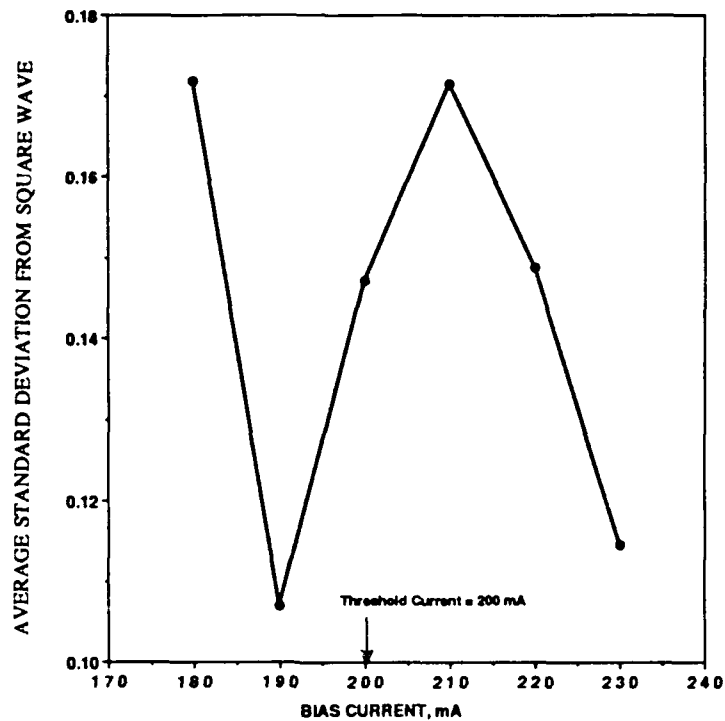


FIGURE 2.13 Average standard deviation from a square wave intensity profile versus the bias current for a 10-stripe laser diode array (modulation depth = 130 mA).

These results can be qualitatively explained by assuming that the position of the gain curve with respect to the mode positions during the pulse plays a role in determining the severity of the transients. In one case the gain curve is centered over one mode, and in another case it is centered between two modes. In the second case the two modes may compete more strongly for power resulting in a longer transient. Gray and Roy⁸ have examined mode stability in AlGaAs laser diodes. They have observed these lasers to operate in different regimes of single-mode behavior (with most of the power concentrated in one mode), bistability (where two modes are lasing but only one at a time) and multimode behavior (with both modes oscillating simultaneously) depending on small changes in operating current and

temperature. They utilize a multidimensional laser model with Langevin noise sources and asymmetric nonlinear gain to model this behavior.

2.2 General discussion of experimental results obtained using the APD

Our experimental data show that two types of modal transients, mode-buildup transients and thermal transients, occur as a result of current injection in a diode laser. The mode-buildup transients occur over a relatively short period of time (10-60 ns) that is dependent on the laser length. They last 10-30 ns for 300 μm length lasers and 20-60 ns for 600 μm length lasers. Thermal transients are distinguishable from mode buildup transients by much longer time constants (on the order of several hundred nanoseconds) and so the modal instabilities caused from these can last several microseconds.

As we have seen, the broad-stripe GRINSCH SQW laser diodes have negligible thermal transients for a modulation depth of 100 mA. The MQW narrow stripe laser had the largest thermal transients. The narrow-stripe SQW laser also had large thermal transients. It was found for our test setup that mode chirping can cause the mode to move out of the detector area during the pulse duration for lasers with thermal transients greater than 0.5 $^{\circ}\text{C}$. For these lasers, an accurate measure of the mode hopping phenomena can only be made either for short pulse durations or at low levels of modulation.

The severity of both the mode-buildup transients and thermal transients is directly related to the modulation depth of the pulse. It was also found that the severity of the modal transients is dependent on the bias current during modulation.

2.3 Determination of the relaxation oscillation frequencies of the laser diodes with a streak camera

The relaxation oscillation frequencies of the laser diodes as a function of modulation current were determined with a streak camera. The relaxation oscillations in the laser are due to the time delay involved in the cyclical process of building up a population inversion and the subsequent stimulated emission that increases the photon number and reduces the carrier population to below the inversion level. The relaxation oscillation frequency also determines the ultimate modulation frequency at which a semiconductor laser can be modulated.

Figure 2.14 shows the experimental configuration used.

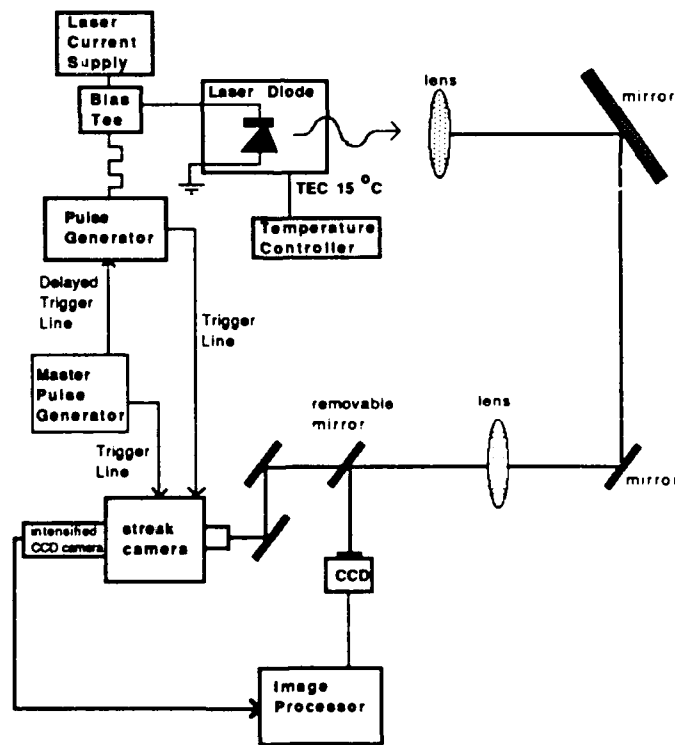


FIGURE 2.14 Streak camera experimental configuration.

With this setup, the laser is square pulse modulated at different depths and its output focused onto the slit of the streak camera. The pulse period was

20 ns with a duty cycle of 0.002%. The pulse generator had a rise time of 150 ps. In a streak camera, photons enter through a slit and are focused onto a photocathode. The photocathode converts the light to electrons which are accelerated down a vacuum tube, optionally amplified with a microchannel plate, and then deflected across a phosphor screen. The phosphor screen is read out with a CCD camera. The streak camera has the advantage that it can observe the relaxation oscillations of the laser diodes with picosecond resolution. It can also perform both single-pulse and multi-pulse measurements. It does have the disadvantage, though, that unless the photocathode obtains fairly large amounts of light the streak image can be noisy.

Figures 2.15 and 2.16 show the streak camera plots for the SQW-5-300 laser and the SQW-60-300 laser taken at modulation depths of 80+143 mA and 0+254 mA, respectively. As can be seen, the narrow stripe laser gives very clear oscillations, whereas the broad stripe laser's oscillations are hard to see and quickly become chaotic. The broad area laser's tendency to oscillate with uncontrolled filamentation probably contributes to this. The filamentation is due to various kinds of nonuniformity, particularly nonuniformities in the epitaxial layers.⁹ This type of behavior has been studied by Yu, et al., in the context of broad area operating laser arrays.¹⁰ Data was taken for all four of the MacDac lasers for a certain range of current around threshold. The oscillation frequency versus $\left(\frac{I-I_{th}}{I_{th}}\right)^5$ is plotted in Figure 2.17. As predicted by theory,^{11,12,13} a straight line relationship is expected, in agreement with our experimental results. The SQW-5-600, SQW-5-600, and SQW-60-600 lasers were pulsed from threshold and the SQW-60-300 laser was pulsed from zero.

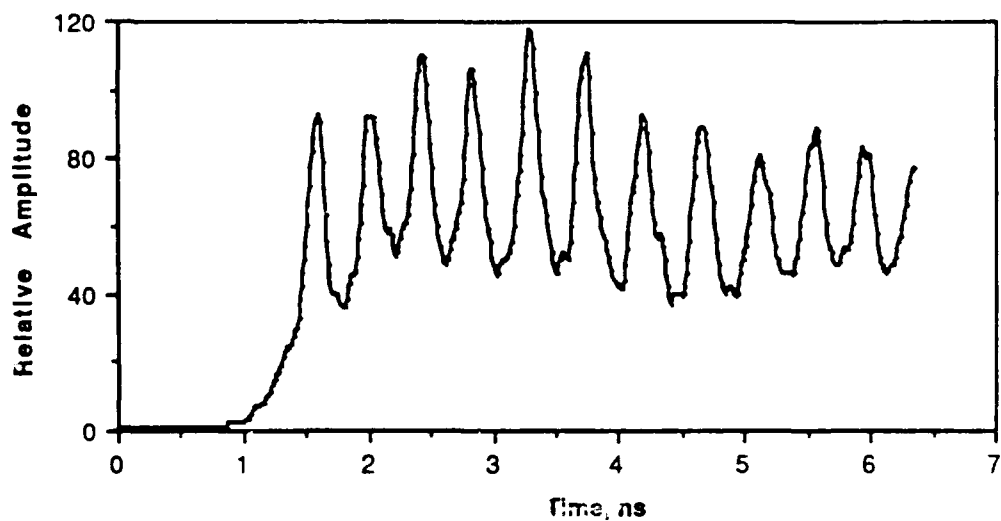


FIGURE 2.15 Streak camera plot of SQW-5-300 laser diode modulated at 80 + 143 mA.

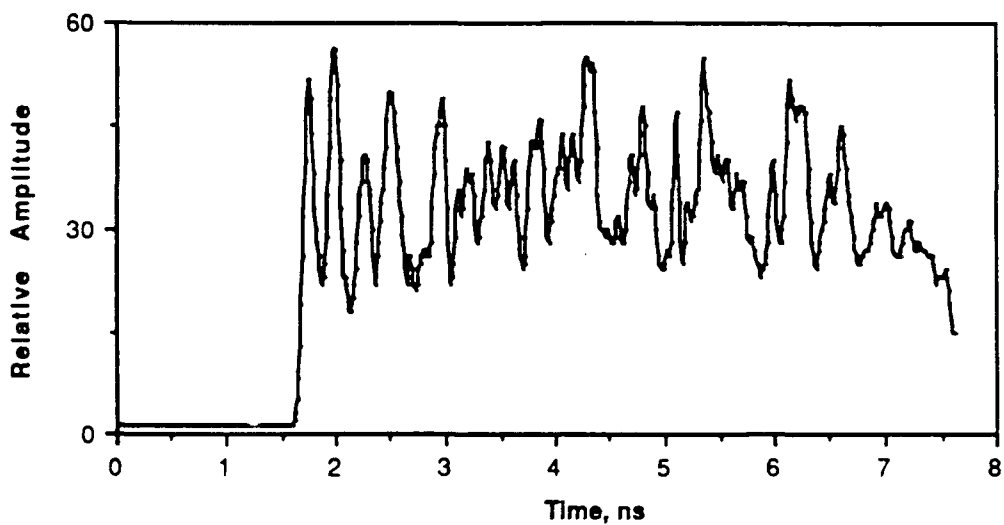


FIGURE 2.16 Streak camera plot of SQW-60-300 laser diode modulated at 0 + 254 mA.

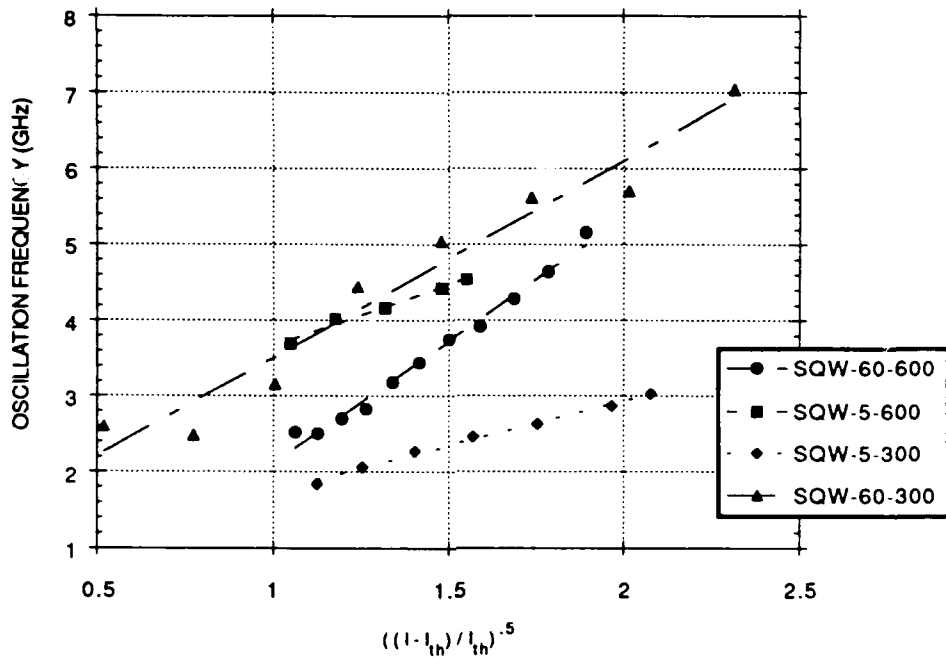


FIGURE 2.17 Oscillation frequency versus normalized current for the GRINSCH SQW laser diodes.

These data can be compared to the results obtained from the rate equation modeling in Chapter 4.

CHAPTER 3

THERMAL MODELING WITH NASTRAN FINITE ELEMENT CODE

3.1 Setting up the NASTRAN finite element code

The NASTRAN finite element code¹⁴ is a software program for modeling temperature transients in different materials due to localized heat sources. It was adapted to simulate temperature transients within the active area of semiconductor lasers. In this model, the diode is divided into a grid of cells. The conductivity, density and heat capacity of the material within each cell are specified as well as any heat generated from photon absorption, non-radiative recombination, or ohmic heating. The model uses the thermal conductivities, the thermal diffusivities and the assumption that heat can flow out only through a constant temperature heat sink to determine the thermal distribution in the laser during modulation or in steady-state operation.^{15,16}

Both 2-dimensional and 3-dimensional modeling of the laser diode and heat sink were used. The laser itself can be accurately modeled two-dimensionally because edge effects are assumed not to be important. Three-dimensional effects of thermal dissipation in the heat sink become a factor as the heat sink thickness is increased beyond about 100 μm . Three-dimensional modeling is very computationally intensive so it was used only to determine the thermal impedance of the heat sink. A thickness for the two-dimensional heat sink was chosen by trial and error until the temperature rise in the heat sink matched the value determined three-dimensionally. The transient analysis was done 2-dimensionally.

Three cases were simulated in this paper, the 60 μm wide broad-stripe laser (SQW-60-300), the 5 μm wide narrow-stripe laser (SQW-5-300), and the

10-stripe laser diode array (MQW-100-250). All lasers were mounted junction-side-down.

Figure 3.1 shows the 2-dimensional grid used in the simulation for the 10-stripe laser array. The heat sink is only partially shown because of its size. The grid was built with variable size cells to reduce the total number of cells and therefore the computational time required to run the simulation. The first 55 horizontal cells are each 1 μm thick. The remaining cells gradually increase in size. The active area of the laser and the layers with large heat fluxes were given smaller grid sizes so the temperature transients could be more accurately modeled in those regions. Only half of the laser was modeled because of symmetry about the vertical axis. The loss of heat into the air was assumed to be negligible. The ambient temperature was fixed at the bottom of the heat sink where heat was allowed to flow out passively. Figure 3.2 shows a full view of the 3-dimensional model used. The 3-dimensional model used larger cell sizes than the 2-dimensional model.

Figure 2.3 shows the composition and layer thicknesses for the 10-stripe laser diode (MQW-100-250). The metallization¹⁷, diode^{18,19,20,21}, and heat sink²² compositions and thicknesses were obtained from several sources. Typically, the active area for a MQW laser consists of four 0.013 μm thick layers of $\text{Ga}_{0.94}\text{Al}_{0.06}\text{As}$ separated by three .004 μm thick layers of $\text{Ga}_{0.8}\text{Al}_{0.2}\text{As}$ ¹⁸. In this work the active area was modeled as a single layer 0.06 μm thick with the average composition of $\text{Ga}_{0.91}\text{Al}_{0.09}\text{As}$. The ten stripes were defined by proton implantation. The heat capacity and conductivity of GaAs were used for the proton-implanted pGaAs (p+GaAs) current-isolating layer. The heat capacities of $\text{Ga}_{0.6}\text{Al}_{0.4}\text{As}$ and $\text{Ga}_{0.91}\text{Al}_{0.09}\text{As}$ were not available and were approximated by doing a linear fit of data between the heat capacity values of GaAs and $\text{Ga}_{0.5}\text{Al}_{0.5}\text{As}$. The 2-dimensional heat sink thickness used was 300 μm , which

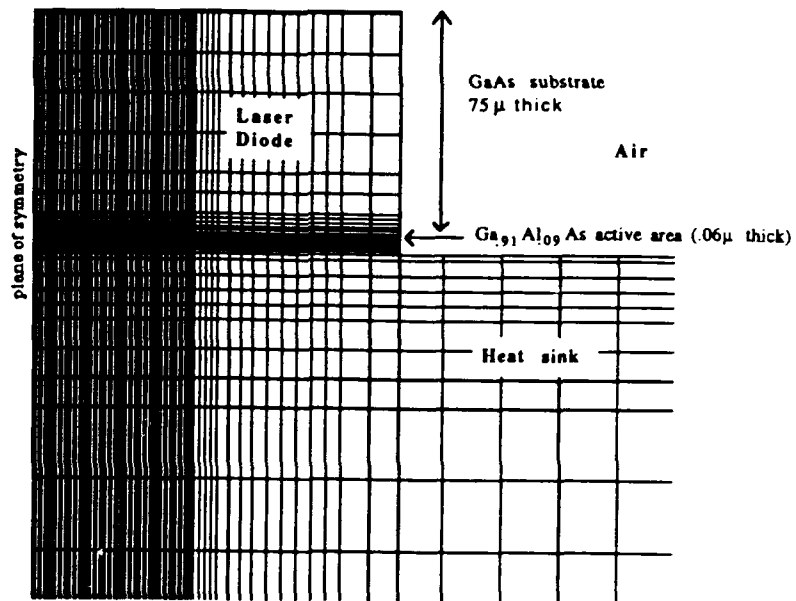


FIGURE 3.1 Two-dimensional finite element grid structure for thermal modeling of laser diode array

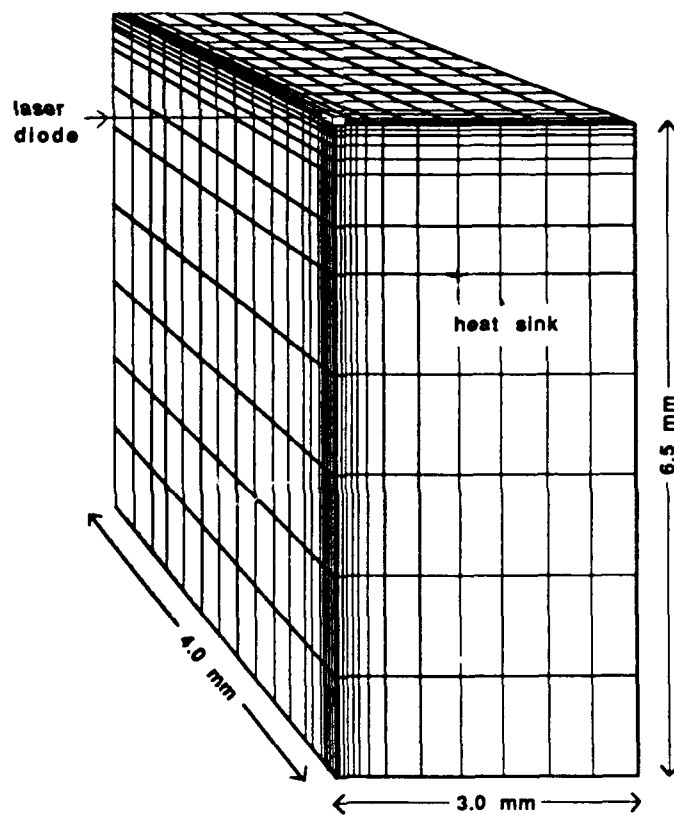


FIGURE 3.2 Three-dimensional grid structure for thermal modeling of laser diode heat sink.

approximately matched the thermal impedance of the 3-dimensional heat sink. The width of the heat sink was 600 μm . The temperature of the heat sink on the bottom row of cells was fixed at 20°C.

Figure 2.2 shows the composition and layer thicknesses for the broad-stripe laser diode (SQW-60-300). The narrow stripe SQW-5-300 laser diode has the same structure but with a 5 μm stripe width instead of a 60 μm stripe width. The stripes are designated by a SiO_2 layer. The thermodynamic properties of the materials present in the lasers are given in Table 3.1.

TABLE 3.1
Thermodynamic Properties

Material	Molecular Weight	Density	Conductivity	Heat Capacity	Heat Capacity	Thermal Diffusivity
	g/gmole	g/cm^3	$\text{W}/(\mu\text{m}\cdot^\circ\text{C})$	cal/ $(^\circ\text{C}\cdot\text{mole})$	$\text{J}/(^\circ\text{C}\cdot\mu\text{m}^3)$	cm^2/sec
Ni	58.71	8.90 ²³	0.91E-4 ²³	6.22 ²³	395.E-14	-
In	114.82	7.30 ²³	0.818E-4 ²³	6.43 ²³	171.E-14	-
Au	196.97	18.88 ²³	3.18E-4 ²³	6.07 ²³	243.E-14	-
Cr	52.00	7.20 ²³	0.939E-4 ²³	5.56 ²³	322.E-14	-
Sn	118.69	6.54 ²³	0.617E-4 ²⁴	6.45 ²³	149.E-14	-
Cu	63.54	8.92 ²³	4.01E-4 ²²	5.84 ²³	343.E-14	-
Ti	47.90	4.5 ²³	0.219E-4 ²³	5.98 ²³	235.E-14	-
Ge	72.59	5.35 ²³	0.602E-4 ²³	5.58 ²³	172.E-14	-
Pt	195.09	21.45 ²³	0.716E-4 ²³	6.18 ²³	284.E-14	-
W	183.85	19.35 ²³	1.73E-4 ²³	5.80 ²³	255.E-14	-
GaAs	144.64	5.31 ²⁵	0.45E-4 ²⁶	11.05 ²³	170.E-14	0.27 ²⁷
Ga _{0.5} Al _{0.5} As	-	-	0.12E-4 ²⁶	-	235.E-14	0.051 ²⁸
Ga _{0.6} Al _{0.4} As	-	-	0.12E-4 ²⁶	-	222.E-14	-
Ga _{0.4} Al _{0.6} As	-	-	0.12E-4 ²⁶	-	248.E-14	-
Ga _{0.7} Al _{0.3} As	-	-	0.13E-4 ²⁶	-	209.E-14	-
Ga _{0.85} Al _{0.15} As	-	-	0.16E-4 ²⁶	-	190.E-14	-
Ga _{0.91} Al _{0.09} As	-	-	0.21E-4 ²⁶	-	182.E-14	-
Ga	69.72	5.904 ²³	-	6.205 ²³	220.E-14	-
Al	26.98	2.702 ²³	2.18E-4 ²⁴	5.82 ²³	244.E-14	-
As	74.922	5.72 ²⁴	0.502E-4 ²³	5.88 ²³	188.E-14	-
SiO ₂	60.08	2.32 ²³	0.01E-4 ²²	10.8 ²⁴	174.E-14	-

3.2 Determination of heat sources within the diode

Heat is generated in the laser diode from ohmic heating at the p-contact, non-radiative recombination in the active layer, photon absorption in the active layer, and photon absorption in the substrate and p-cap layer.^{22,29,30,6,12}

The equations in Table 3.2, derived in a paper by Kobayashi and Furukawa³⁰, are used to calculate the heat input to the various layers of the diode.

TABLE 3.2
Equations for Calculating Heat Input in the Laser Diode

below threshold ($I < I_{th}$)	above threshold ($I > I_{th}$)	Layer
$V_j I (1 - \eta_{spon}) + V_j I \eta_{spon} (1 - f)$	$(V_j I - V_j I_{th})(\eta_i - \eta_{ext}) + V_j I_{th} \eta_{spon} (1 - f) + V_j I_{th} (1 - \eta_{spon}) + (V_j I - V_j I_{th})(1 - \eta_{spon}) \eta' + (V_j I - V_j I_{th})(1 - f) \eta' \eta_{spon}$	active layer
$V_j I \eta_{spon} f/2$	$V_j I_{th} \eta_{spon} (f/2) + (V_j I - V_j I_{th}) \eta' \eta_{spon} (f/2)$	GaAs substrate
$V_j I \eta_{spon} f/2$	$V_j I_{th} \eta_{spon} (f/2) + (V_j I - V_j I_{th}) \eta' \eta_{spon} (f/2)$	p-GaAs cap layer
$I^2 R_s$	$I^2 R_s$	each layer except active layer

In these equations, V_j is the junction voltage, η_i is the internal efficiency of lasing, R_s is the series resistance of each layer, η_{spon} is the internal quantum efficiency of the spontaneous emission, $\eta' = 1 - \eta_i$, I_{th} is the threshold current, η_{ext} is the external differential quantum efficiency of lasing, I is the current, and f is the fraction of spontaneous emission radiated from the active layer and absorbed by the GaAs substrate and p-GaAs cap layer. The value f is approximately equal to $1 - (1 - (n_1/n_0)^2)^{-5}$, where n_0 and n_1 are the refractive indices of the active layer and the cladding respectively.²²

For $\eta_i=1$ ($\eta'=0$) and $\eta_{\text{sp0n}}=1$, assuming ohmic heating to occur primarily at the p-contact metallization layer²², the equations reduce to those shown in Table 3.3.

TABLE 3.3
Simplified Equations for Calculating Heat Input in the Laser Diode

at threshold ($I=I_{th}$)	above threshold ($I>I_{th}$)	Layer
$V_j I_{th} (1-f)$	$(V_j I - V_j I_{th})(1-\eta_{ext}) + V_j I_{th}(1-f)$	active layer
$V_j I_{th} f/2$	$V_j I_{th}(f/2)$	GaAs substrate
$V_j I_{th} f/2$	$V_j I_{th}(f/2)$	p-GaAs cap layer
$I_{th}^2 R_s$	$I^2 R_s$	p-contact layer

The operating parameters for the diodes are given in Table 3.4. The operating parameters for the MQW lasers were obtained from their data sheets. The operating parameters for GRINSCH SQW lasers were obtained from D.K. Wagner, et. al.² and data sheets. V_{b1} is the diode voltage at threshold, and V_{b2} is the diode voltage at the operating current above threshold. The narrow-stripe laser has a higher ohmic resistance because of the smaller contact area.

TABLE 3.4
Operating Parameters for Laser Diodes

Parameter	SQW-60-300		MQW-100-250		SQW-5-300
	broad-stripe		10-stripe		1-stripe
Optical power (mW)	80	200	100	200	46
V_j (V)	1.51	1.51	1.51	1.51	1.51
V_{b1} (V)	1.54	1.54	1.76	1.76	-
V_{b2} (V)	1.63	1.78	1.81	1.9	-
I_{th} (mA)	100	100	200	200	75
I (mA)	200	340	340	475	128
R_s (Ω)	.6	.6	.85	.85	6
f	.65	.65	.65	.65	.65
η_{ext}	.473	.473	.49	.49	.62

When the operating parameters of Table 3.4 are substituted into the equations of Table 3.3, the generated heat in the specified layers of the laser can be found. These values are listed in Table 3.5. The listed values for total heat generated represent the total power into the laser minus the optical power output. For a 10-stripe laser, each stripe will receive only one tenth of these power levels. The broad-stripe lasers are more efficient than the 10-stripe array because current spreading is not as significant for them. It occurs only at the two outer edges of the broad active area as opposed to on either side of each stripe for the 10-stripe laser.

TABLE 3.5
Heat Generated in the Laser Diode (in Watts)

Parameter	SQW-60-300		MQW-100-250		SQW-5-300
Laser type	broad-stripe		10-stripe		1-stripe
Optical power (mW)	80	200	100	200	46
at threshold:					
active layer	0.0529	0.0529	0.106	0.106	0.040
GaAs substrate	0.049	0.049	0.098	0.098	0.037
p-GaAs cap layer	0.049	0.049	0.098	0.098	0.037
p-contact layer	0.006	0.006	0.034	0.034	0.034
above threshold:					
active layer	0.132	0.244	0.214	0.317	0.070
GaAs substrate	0.049	0.049	0.098	0.098	0.037
p-GaAs cap layer	0.049	0.049	0.098	0.098	0.037
p-contact layer	0.024	0.069	0.098	0.192	0.098
Total heat generated					
at threshold:	0.157	0.157	0.336	0.336	0.147
above threshold:	0.255	0.411	0.508	0.706	0.241

For the MQW-100-250 and SQW-5-300 lasers the current in the active layer spreads out laterally, increasing the effective stripe width. Determination of the actual current distribution in the diode's active area was

accomplished by powering the laser below the threshold current and imaging the laser facet onto a CCD camera.²² The CCD camera is interfaced with an image processor which can plot the intensity distribution of the spontaneous emission. The assumption was made that the output intensity distribution is proportional to the current distribution. For the MQW-100-250 array, with cell widths of 1 μm the fraction of power per cell was measured to be 0, 0.03, 0.10, 0.17, 0.20, 0.20, 0.17, 0.10, 0.03, 0 across the ten active layer cells for a current 10 mA below threshold. This profile was also used as an approximation for the substrate and cap layers. For the broad-stripe laser, because the stripe is wide and the central portion of the stripe was the area of interest, no current spreading was used in the simulation. For the SQW-5-300 narrow-stripe laser a Gaussian distribution was seen with a full width half maximum (FWHM) of 20 μm at a current 13% of threshold. This FWHM decreased as the current increased, with a FWHM of 15 μm for a current 31% of threshold, a FWHM of 10 μm for a current 44% of threshold, a FWHM of 7 μm for a current 67% of threshold, and a FWHM of 5.5 μm for a current 91% of threshold. The current distribution above threshold cannot be accurately measured by imaging because the lasing regions will show disproportionately more intensity than the non-lasing regions because the lasing light is directional. For this work, the value of 5 μm for the FWHM was used to model the SQW-5-300 narrow-stripe laser.

3.3 Steady-state results

Table 3.6 shows the change in temperature of the active area in the center of the stripe from the heat sink temperature of 20 °C for the three laser diodes for various current levels run at steady-state.

TABLE 3.6

Change in Temperature of Active Area during Steady-State Operation

Laser	Optical Power (mW)	Temperature Rise, °C
SQW-60-300	80	4.78
	200	7.60
MQW-100-250	200	10.7
SQW-5-300	46	10.24

3.4 Transient results and discussion

Table 3.7 lists the temperature change of the active area in the center of the stripe for the three lasers during modulation with 80 ns and 1600 ns pulses. For the 80 ns pulse, a 50% duty cycle was used. For the 1600 ns pulse, the laser was set initially at the threshold current level until the temperature reached steady state and then the modulating current was applied. This approximates a 50% duty cycle pulse since in 1600 ns the temperature in the active region will have a long enough time to settle back to the threshold temperature after the modulated pulse ends. The transient simulations were run with varying step sizes. The first section was run with a step size of 9 μ s to bring the diode near steady state. After that, a step size of 1 ns was used.

TABLE 3.7

Thermal Transients in Active Area of Pulsed Laser Diodes

Laser	Peak Power, mW	Temperature Rise, C (80 ns pulse)	Temperature Rise, C (1600 ns pulse)
SQW-60-300	80	.092	.58
	200	.219	-
MQW-100-250	200	0.35	-
	100	0.18	-
SQW-5-300	46	0.396	2.12

The SQW-60-300 broad-stripe laser has smaller transients than the MQW-100-250 ten-stripe array because it has minimal current spreading. It also has a larger total active area (60 μm versus 40 μm for the 10-stripe laser), and has a longer length of 300 μm versus ~250 μm for the 10-stripe laser. Figure 3.3 plots the temperature in the active area of the laser during modulation for the SQW-60-300 laser for a peak optical power of 80 mW and 80 ns pulses. Figure 3.4 shows the SQW-60-300 laser with a peak optical power of 80 mW for a 1600 ns pulse.

These temperature transients can be translated into modal transients and compared to experimental data by using the relationship that the emission wavelength for a typical GaAlAs laser will shift an average of ~3 Å/°C.⁴

Table 3-8 shows the thermal time constants of the transients fitted to the equation

$$\Delta T(t) = (k_1(1-e^{-t/T_1})+k_2(1-e^{-t/T_2})) \quad (3.1)$$

where $\Delta T(t)$ is the temperature rise, t is the time in ns, and k_1 and k_2 are steady state temperature values associated with the time constants T_1 and T_2 .

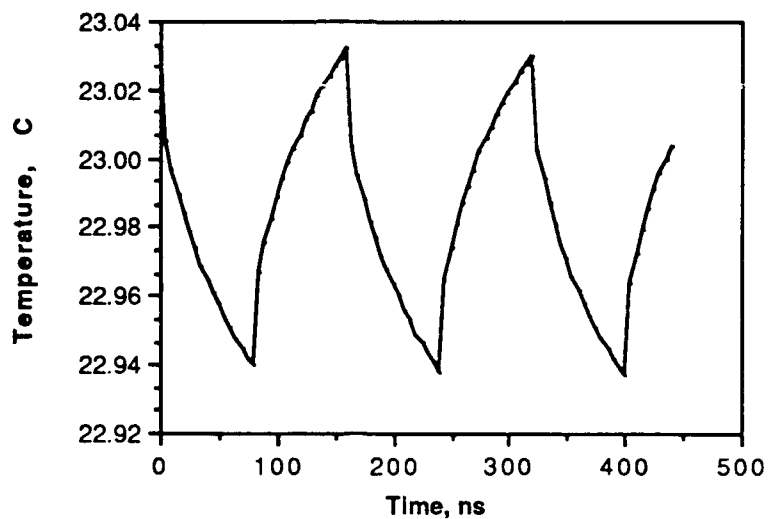


FIGURE 3.3 Thermal transients in active area of SQW-60-300 laser during modulation with a 160 ns square wave and 80 mW peak optical power.

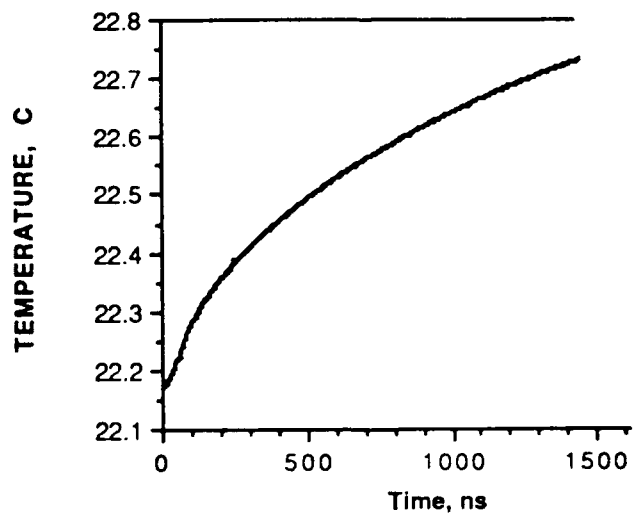


FIGURE 3.4 Thermal transients in active area of SQW-60-300 laser during modulation with a 1600 ns pulse and 80 mW peak optical power.

TABLE 3-8

Thermal Time Constants Fitted to Transient Data from the Finite Element Code
Analysis

Laser	Transient Time, ns	Output Power, mW	k 1 (C)	T1 (ns)	k 2 (C)	T2 (ns)
SQW-60-300	80	80	0.0281	4.5	0.091	70
	1600	80	0.295	400	0.41	1500
SQW-5-300 FWHM=5	80	46	0.16	7	0.45	110
	1600	46	0.8	220	2.1	1600

3.5 Effect of varying cell sizes

The cell size was varied for the lasers to determine its effect on the simulations. In one case, cell widths of 1 μm were used with cell thicknesses of 0.5 μm in the confinement area. In the other case cell widths of 0.1 μm were used with cell thicknesses of 0.05 μm in the confinement area. Small changes in the thermal transients on the order of a few percent occurred, indicating that accurate simulations can be made with the larger cell sizes.

CHAPTER 4

TEMPERATURE-DEPENDENT RATE EQUATIONS MODEL

4.1 Introduction

Rate equations model the modal output power characteristics of laser diodes. The characteristics and dimensions of the laser are entered into the program along with the driving current, and the equations are solved numerically to predict the power in each of the laser modes as a function of time. The rate equations model is used to obtain information on relaxation oscillation frequency, modal power distribution, total output power, and the settling times of the modal power fluctuations due to mode-buildup time transients and thermal-induced transients.

Temperature-independent rate equations have been described by many workers in the field including Marcuse and Lee³¹, Yariv³², Adams and Osinski³³, and Agrawal and Dutta³⁴. Byrne and Keating have developed temperature-dependent rate equations by adding temperature dependence to the threshold current density and to the peak of the modal gain curve distribution, however, they only investigated dc behavior.³⁵ This report uses the equations developed by Byrne and Keating and extends their work by examining transient behavior.

4.2 Description of Rate Equations

The electron and photon transient behavior in laser diodes can be described by the following rate equations,

$$\frac{dn_e}{dt} = \frac{j}{ed} - \frac{n_e}{\tau_e} - \sum_{\nu=-n/2}^{n/2} M A D_{\nu} (n_e - \hat{n}_0) s_{\nu} \quad (4.1)$$

$$\frac{ds_{\nu}}{dt} = \frac{\Gamma \gamma}{\tau_r} D_{\nu} n_e - \frac{1}{\tau_p} s_{\nu} + M \Gamma A D_{\nu} (n_e - \hat{n}_0) s_{\nu} \quad (4.2)$$

The variables in these equations are defined as follows:

- n_e = injected electron density in the conduction band, μm^{-3}
- t = time coordinate, s
- j = current density, A/cm^2
- e = electron charge (1.6×10^{-19} C)
- d = thickness of active laser region, μm
- τ_e = carrier lifetime, s
- τ_r = carrier lifetime due to radiative recombination processes
- $n+1$ = number of modes with gain
- A = stimulated emission factor, $\mu\text{m}^3/\text{s}$
- D_{ν} = line shape factor
- \hat{n}_0 = carrier density for transparency, μm^{-3}
- s_{ν} = photon density of ν th laser mode, μm^{-3}
- Γ = ratio of active layer volume to optical mode volume (mode confinement factor)
- γ = fraction of spontaneous emission coupled into the lasing mode (assumed to be frequency independent)
(spontaneous emission factor)
- τ_p = photon lifetime, s
- M = gain saturation term

The photon lifetime, τ_p , is related to the group refractive index of the laser medium, n_g , and the effective cavity loss coefficient, α , by the relation

$$\tau_p = n_g / (c \alpha) . \quad (4.3)$$

The photon lifetime represents the average time the photon spends in the cavity. It takes into account cavity losses due to absorption of photons in the cavity and mirror losses. The effective cavity loss coefficient, α , is related to the cavity length and reflectivity of the mirrors, R , by

$$\alpha = \alpha_i + \frac{1}{L} \ln \frac{1}{R} , \quad (4.4)$$

where $R = \sqrt{R1 \cdot R2}$ and $R1$ and $R2$ are the intensity reflectivity coefficients (reflectances) for the front and back facets. The reflectance, $R1$, is approximately 0.32 for an uncoated facet.² The intrinsic loss coefficient is α_i .

The gain compression term, M , is defined as

$$M = \frac{1}{1 + \sum_{\nu=-n/2}^{n/2} \epsilon s_{\nu}} \quad (4.5)$$

where ϵ is the gain compression factor. The main effect of the gain compression term is to dampen the relaxation oscillations of the laser. The gain compression term (sometimes referred to as gain saturation factor) is a phenomenological term which takes into account various nonlinearities occurring in the laser medium and spectral hole burning.^{36,37} It has also been used to represent the effect of lateral carrier diffusion in narrow width

lasers.^{38,39} The transient response is not very sensitive to the exact value of the gain saturation factor (other than damping the relaxation oscillations). Values for ϵ could not be derived accurately from the experimental data in this report, though, in Chapter 5, approximate values for ϵ are found which moderately dampen the relaxation oscillations for the various lasers.

Equation (4.1) can be normalized by multiplying through each side by $\tau_p A$ as shown in equation (4.6). Equation (4.2) is normalized by $\tau_e A$ as shown in equation (4.7). The assumption is made that τ_r is approximately equal to τ_e as will be discussed later in Section 4.10.

$$\frac{d(n_e \tau_p A)}{dt} = \frac{j \tau_p A}{e d} - \frac{(n_e \tau_p A)}{\tau_e} - \sum_{v=-n/2}^{n/2} D_v \{(n_e \tau_p A) - (\hat{n}_0 \tau_p A)\} \frac{M(s_v \tau_e A)}{\tau_e} \quad (4.6)$$

$$\frac{d(s_v \tau_e A)}{dt} = \frac{\Gamma \gamma}{\tau_p} D_v (n_e \tau_p A) - \frac{1}{\tau_p} (s_v \tau_e A) + \Gamma D_v \{(n_e \tau_p A) - (\hat{n}_0 \tau_p A)\} \frac{M(s_v \tau_e A)}{\tau_p} \quad (4.7)$$

Using the equalities

$$N = n_e \tau_p A,$$

$$S_v = s_v \tau_e A,$$

$$N_0 = \hat{n}_0 \tau_p A,$$

$$J_n = \frac{j \tau_e \tau_p A}{e d},$$

we obtain the following equations,

$$\frac{dN}{dt} = \frac{1}{\tau_e} \left(J_n - N - \sum_{v=-n/2}^{n/2} M D_v (N - N_0) S_v \right) \quad (4.8)$$

$$\frac{dS_v}{dt} = \frac{1}{\tau_p} (\Gamma \gamma D_v N - S_v + M \Gamma D_v (N - N_0) S_v). \quad (4.9)$$

The normalization of the electron and photon density equations not only serves to simplify the equations but also facilitates the use of a Runge-Kutta numerical analysis. This is because the stiffness of the equations is determined by the ratio of the independent variables. The ratio of the electron density over the photon density is normally quite high so the equations are stiff and require a very small time step to converge. The normalization factors reduce the ratio of the electron and photon density terms and so the system converges with a much larger time step.

The first term in (4.1) is the increase in electron carriers due to current. The second term is the decrease in electron carriers due to spontaneous emission, and the third term is the decrease or increase in electron carriers due to stimulated emission or absorption of photons.

Equation (4.2) represents the change in photon population for each separate guided mode. The first term in (4.2) is the increase in the photon population due to spontaneous emission. The factor γ accounts for the fact that only a fraction of the spontaneously emitted photons contribute to the guided mode. The second term represents the loss of photons due to cavity losses. The third term represents the stimulated emission or absorption of photons. Note that the stimulated emission rate represented by this term is due both to a gain factor and to the concentration difference of electrons above transparency and the concentration of photons in that particular mode. As described in Section 2.1, it is the fact that the stimulated emission rate is driven by the concentration of photons in a particular mode that causes the mode-buildup transients. It is only because of feedback that the power tends to gradually

concentrate in a few dominant modes. The first and third terms of (4.2) are multiplied by Γ to account for the different volumes occupied by the electrons and photons. This can be verified by holding Γ constant and iterating the rate equations for different values of active layer thicknesses. The optical power out of the cavity is independent of the active layer thickness as long as Γ stays constant.

The photon density can be converted into optical power out of the laser cavity as shown in the following equation:

$$P = \sum_{v=-n/2}^{n/2} s_v \frac{L S d}{\Gamma} E \frac{1}{n_g / (c(\alpha - \alpha_i))} \quad (4.10)$$

where

$$E = \frac{h c}{\lambda_{p0}}$$

and the variables are defined as

- P = optical power, W
- S = width of laser stripe, μm
- L = cavity length, μm
- E = energy per photon, J
- h = Planck's constant (6.626×10^{-34} J/s)
- c = velocity of light in vacuum (3×10^{14} $\mu\text{m/s}$)
- λ_{p0} = wavelength at the peak of the mode distribution at time 0
- $\alpha - \alpha_i$ = facet loss = $\frac{1}{L} \ln \frac{1}{R}$.

In (4.10), the photon density is multiplied by the mode volume and energy per photon to give the energy in joules represented by all the photons

in the cavity. This energy is then divided by the photon lifetime (without internal losses) to give the optical power coming out of the cavity.

4.3 Determination of the stimulated emission factor and the transparency electron current density

The stimulated emission factor, A , affects the oscillation frequency of the relaxation oscillations. A larger stimulated emission factor increases the oscillation frequency. The stimulated emission factor can be obtained through values obtained for the gain. In Thompson⁶ and Kressel and Butler^{1,2} the theoretical relation between peak optical gain, g , in cm^{-1} , and injected current density, J , in Amps cm^{-2} , for pure GaAs at various temperatures is

$$g = \beta(J - J_0) \quad (4.11)$$

where J_0 is the transparency electron current density. The gain, g , is defined as the power emitted per unit volume divided by the power crossing per unit area.^{1,2} If this relation is plotted, the slope of the line represents the gradient β (sometimes referred to as the differential gain coefficient) in cm Amp^{-1} . The relationship between β and the stimulated emission factor, A , is given by

$$A = \frac{\beta d \epsilon c}{\tau_e n_g} \quad (4.12)$$

The transparency electron density for the peak mode of the distribution is related to the transparency electron current, J_0 , by the relation^{1,2}

$$\hat{n}_0 = \frac{J_0}{ed} \tau_e \quad (4.13)$$

The actual threshold current of the device can be determined by the threshold condition where the gain equals the loss²,

$$\Gamma g = \alpha_i + \frac{\ln(1/R)}{L}, \quad (4.14)$$

and the gain current relation (4.11). The expression derived from these two equations is

$$I_{th} = \frac{S}{\eta_i} \left((J_0 + \frac{\alpha_i}{\Gamma \beta}) L + \frac{\ln(1/R)}{\Gamma \beta} \right), \quad (4.15)$$

where I_{th} is the threshold current during the pulse in Amps.

In narrow stripe gain-guided laser diodes the current will not remain confined to the narrow stripe width defined by the oxide or proton implantation. There are two processes by which this occurs. First, the current will spread out during its trip from the metal contact down to the active area. This effect is directly related to the current density, and the thickness and conductivity of the confining layer which comes between the active layer and the metallization. Once the current reaches the active layer, it will diffuse outward along the active region. This effect is related to the diffusivity and to the carrier lifetime in the active region.

Casey and Panish⁴⁰ have derived equations that predict the carrier distribution in the laser diode active layer based on both current spreading and active-layer carrier diffusion. They combine the current spreading expressions described by Yonezu *et. al.*⁴¹ with the carrier-diffusion model of

Hakki⁴², Thompson⁶ and Streifer, et.al.,⁴³ also describe the effects of current spreading and diffusion.

In the Casey and Panish approach, current spreading effects are characterized by a current spreading length,

$$l_0 = \frac{2L}{\kappa \rho_s I_0} \quad (4.16)$$

where
$$I_0 = \frac{(1 + (S\kappa\rho_s/(2L))I_t)^{.5} - 1}{S\kappa\rho_s/(2L)},$$

and
$$\frac{1}{\rho_s} = \frac{1}{(\rho_1/d_1)} + \frac{1}{(\rho_2/d_2)}.$$

Here I_0 is the lateral spreading current, I_t is the total current, ρ_s is the composite sheet resistivity, d_1 and d_2 are the lengths of the layers through which the current flows to reach the active layer with their respective resistivities, ρ_1 and ρ_2 , and κ is the exponential junction parameter e/nkT . In the SQW lasers used in this report, the confining layer on the p-side is $Ga_{.6}Al_{.4}As$. Using a mobility, μ_p , of $250 \text{ cm}^2/(\text{V s})$ ⁴⁴, and hole doping, p , of $2 \times 10^{17} \text{ cm}^{-3}$, this give a conductivity ($g = \mu_p p e$) of 8 mho cm^{-1} . The resistivity is the inverse of the conductivity. For a thickness, $d_1 + d_2$, of $1.7 \text{ }\mu\text{m}$, stripe width, S , of $5 \text{ }\mu\text{m}$ and stripe length, L , of $300 \text{ }\mu\text{m}$, this makes a characteristic spreading length of $1.2 \text{ }\mu\text{m}$ for a current density of 8500 A/cm^2 , $1.64 \text{ }\mu\text{m}$ for a current density of 5000 A/cm^2 (threshold for the SQW-5-300 narrow stripe laser), $2.12 \text{ }\mu\text{m}$ for a current density of 3330 A/cm^2 , and $6.68 \text{ }\mu\text{m}$ for a current density of 670 A/cm^2 . Also, it should be noted that for proton-bombarded stripe-geometry lasers (such as the MQW-4-250 laser) lateral current spreading is further decreased.⁴⁵

Diffusion effects in the active layer are characterized by a diffusion length. The diffusion length can be calculated knowing the electron mobility, μ_e , and the electron lifetime in the p-type material, τ_p :

$$L_n = (D_e \tau_p)^{.5} \quad (4.17)$$

where
$$D_e = \frac{\mu_e k T}{e}$$

is the diffusion constant, k is the Boltzman constant, $1.38 \cdot 10^{-23}$ J/K, and T is the temperature in degrees Kelvin.⁴⁶ For electrons in GaAs at concentrations below 10^{15} cm^{-3} , μ_e is $0.85 \text{ m}^2/(\text{V sec})$.^{46,12} (This value will decrease at higher electron concentrations.) Using this value, a temperature of $300 \text{ }^\circ\text{K}$, and an electron lifetime of 2 ns^{11} , a value of $6.6 \text{ } \mu\text{m}$ is calculated for the diffusion length. Hakkı⁴² and Streiffer⁴³ use values of 5 and $3 \text{ } \mu\text{m}$, respectively, for the diffusion length when modeling current diffusion in GaAs lasers.

For stripe widths under 20 microns, electron spreading and diffusion effects start playing a major role in the mode size and efficiency and so values of β and J_0 determined from wide width laser diodes are no longer valid. The effect of current spreading and diffusion on the gain factors can be determined by first predicting the profile of the current along the stripe. Then new effective values of β and J_0 for the case of narrow stripe lasers can be calculated. Casey and Panish predict the electron concentration in the active layer. Their equations can be normalized to give the following two equations:

$$J_r(x) = \left(1 - \frac{L_n}{l_0 + L_n}\right) \exp\left(\frac{-S}{2L_n}\right) \cosh\left(\frac{x}{L_n}\right) \left(1 + \frac{2l_0}{S}\right)^{-1} \quad \text{for } |x| < \frac{S}{2}, \quad (4.18)$$

$$J_r(x) = \left(1 + \frac{2l_0}{S}\right)^{-1} \left(1 + \coth\left(\frac{S}{2L_n}\right)\right)^{-1} \left(1 - \left(\frac{l_0}{l_0^2 - L_n^2}\right) \left(l_0 + L_n \coth\left(\frac{S}{2L_n}\right)\right)\right) \exp\left(\frac{-(x-S/2)}{L_n}\right) \\ + \frac{l_0^2}{l_0^2 - L_n^2} \exp\left(\frac{-(x-S/2)}{l_0}\right) \left(1 + \frac{2l_0}{S}\right)^{-1} \quad \text{for } |x| > \frac{S}{2} \quad (4.19)$$

where $J_r(x)$ is the relative percentage of current density at any distance x from the center of the stripe.

Figure 4.1 shows $J_r(x)$ versus x for a stripe width, S , of 5 μm , diffusion length, L_n , of 5 microns and a spreading length, l_0 , of 1.2 μm .

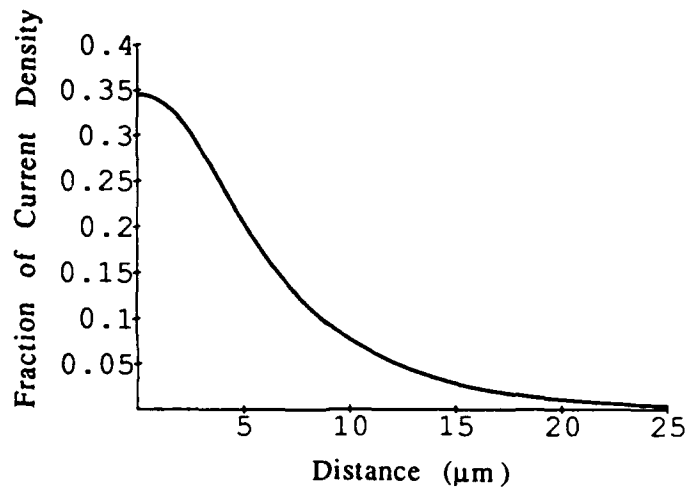


FIGURE 4.1 Relative current density versus distance.

Equations (4.18) and (4.19) can be used to solve for the new gain relationship with modified values of β and J_0 , represented by β^* and J_0^* ,

$$g = \beta^*(J - J_0^*). \quad (4.20)$$

This is done by solving for the gain as a function of distance from the stripe center and current density through the stripe contact, J_{tot} ,

$$\text{gain}(x, J_{tot}) = \beta (Jr(x) J_{tot}) - J_0. \quad (4.21)$$

The effective gain will then be the average gain over the region where there is gain:

$$\text{gain}_{eff}(J_{tot}) = \frac{1}{x_{eff}} \int_0^{x_{eff}} \text{gain}(x, J_{tot}) dx \quad (4.22)$$

where x_{eff} is the distance from the center of the stripe to the point where the gain becomes zero. Equation (4.22) makes the approximation that there is a uniform density of photons in the region where there is gain. The effective gain can be found for other values of J_{tot} and then plotted. The slope of the curve gives the new value of β^* , the gain coefficient, and the x-intercept the new transparency current density, J_0^* .

Figure 4.2 shows the new gain curve plotted along with the gain curve for no current diffusion as a function of current density. This is for the case of $S = 5 \mu\text{m}$, $L_n = 5 \mu\text{m}$, $l_0 = 1.2 \mu\text{m}$, $\beta = 4.4 \text{ cm/A}$, and $J_0 = 145 \text{ A/cm}^2$. The β and J_0 values are taken from values determined for the SQW-60-300 laser.²

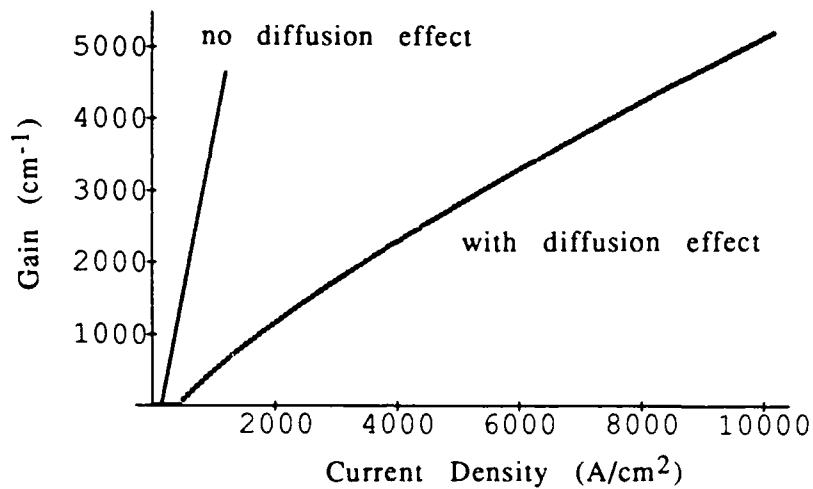


FIGURE 4.2 Gain versus current density through the stripe contact.

From Figure 4.2 the new effective gain parameters, β^* and J_0^* , representing the slope and x-intercept of the curve, can be found. Since the graph only approximates a straight line these values must be interpolated. It is apparent that current spreading through the stripe for a narrow stripe width has dramatic effects on the effective gain of the laser. Table 4.1 lists values for the effective gain parameters calculated for varying spreading and diffusion lengths.

TABLE 4.1

Effective Gain Parameters for Various Diffusion Lengths and Stripe Widths

Diffusion Length (μm)	Spreading Length (μm)	Stripe Width (μm)	β (cm/Amp)	J_0 (Amp/cm ²)	β^* (cm/Amp)	J_0^* (Amp/cm ²)
5	1.2	5	4.4	145	0.51	225
7	1.2	5	"	"	0.415	250
7	3	5	"	"	0.39	325
8	5	5	"	"	0.32	375

4.4 Line shape factor and the gain spectral linewidth

The line shape factor is a Lorentzian equation given as

$$D_v = \frac{1}{1 + [(\lambda_v - \lambda_p(t)) / \Delta\lambda_D]^2} \quad (4.23)$$

where

$\Delta\lambda_D$ = effective gain spectral linewidth parameter, μm

$\lambda_p(t)$ = wavelength at the peak of the gain spectrum for time t

λ_v = wavelength of the v th laser mode.

The spacing between adjacent modes in a cavity, $\Delta\lambda_c$, is determined by

$$\Delta\lambda_c = \lambda_{p0}^2 / (2n_g L). \quad (4.24)$$

The linewidth parameter, $\Delta\lambda_D$, has the effect of determining the steady-state relative power distribution between the modes. The line shape factor equation is determined by fitting the Lorentzian equation to the calculated and measured spontaneous emission spectra of QW GaAs lasers.⁴⁷⁻⁵⁰

4.5 Characterization of the spontaneous emission factor

Of the total spontaneous emission emitted in all directions, only a small portion becomes amplified by the laser modes. This fraction is given by the spontaneous emission factor, γ ,^{51,31,52,53}

$$\gamma = \frac{K\Gamma\lambda_{p0}^4}{4\pi^2 n_r^2 n_g D d L \Delta\lambda_D} \quad (4.25)$$

where K is the astigmatism factor and n_r is the effective refractive index of the laser medium. The factor γ is the ratio of the volume occupied by one guided mode relative to the whole volume receiving photons by spontaneous emission.

The astigmatism factor is used to account for changes in γ due to laser geometry. As will be discussed in Chapter 5, K is affected by laser length and width. It also changes depending on whether the laser is gain- or index-guided.

The spontaneous emission factor affects the mode power distribution. A larger γ causes a larger spread of the power distribution of the modes. The spontaneous emission factor also affects the time it takes for the modal power sharing to settle, with a smaller γ causing the modes to take longer to stabilize in power.

4.6 Incorporation of temperature effects

The peak wavelength of the gain curve is dependent on the current density³³ and on temperature as shown in the following equation,

$$\lambda_v - \lambda_p(t) = u \left(1 - \frac{n_e(t)}{\hat{n}_0} \right) + \delta\lambda_{pt}(t) + \Delta\lambda + (v * \Delta\lambda_c). \quad (4.26)$$

In this equation, $\Delta\lambda$ is the initial detuning of the gain peak from the dominant mode (from $0-0.5 \Delta\lambda_c$), and u is a constant relating the carrier density to the shift in the gain peak (typically 106.4 nm)³³. λ_v and $\lambda_p(t)$ were defined earlier as the wavelength of the v th laser mode and the wavelength at the peak of the

mode distribution for time t . The thermal shift of the peak wavelength of the gain curve, $\delta\lambda_{pt}(t)$, is defined as

$$\delta\lambda_{pt}(t) = h \Delta T(t) , \quad (4.27)$$

where h is the experimental shift of wavelength per $^{\circ}\text{C}$. $\Delta T(t)$ is the temperature shift in the active area previously described by equation (3.1). The gain peak shifts due to carrier density changes and thermal changes are both positive, i.e., the gain peak shifts to longer wavelengths.

The carrier density term becomes zero at threshold because at threshold and at higher modulation levels the carrier density stays constant except for some minor oscillations. Therefore, the factor u in (4.26) which relates the shift in the gain peak due to carrier density changes has minimal effect in the modeling done in this report since the lasers were all pulsed from threshold. The carrier-induced index change and its corresponding wavelength shift is also described by Manning, Olshansky and Su.⁵⁴

The change in temperature over time, $\Delta T(t)$, is determined either experimentally or with a finite element analysis of the thermal transients in the active area of the laser diode during a pulse.^{15,16} To determine $\Delta T(t)$ experimentally, the modes of the pulsed laser diode are separated with a spectrometer and the shift in the gain curve peak during the pulse determined. This needs to be done for each separate laser at each power level. A plot of the shift in the gain curve with time can be made and the data fitted to two thermal time constants, $T1$ and $T2$, where $T1$ is a short thermal time constant, and $T2$ is a long time constant. The temperature increase in the active layer for time constant $T1$ is $k1$ and the temperature increase in the

active layer for time constant T_2 is k_2 . Alternately the change in temperature over time, $\Delta T(t)$, can be determined with a finite element thermal analysis of the diode as discussed previously in Chapter 3.

The output curves from the rate equation analysis in this paper are compared by the use of their time constants. The time constant of the curve comes from the equation

$$\Delta T(t) = T_{\text{final}} [1 - e^{(-t/\tau)}] . \quad (4.28)$$

When t equals τ the value is at 63.2% of T_{final} , its final value. When t equals 2τ the value is at 86.5% of its final value.

The threshold current dependence on temperature is defined as²

$$I_{\text{th}}(t) = I_{\text{tho}} e^{[\Delta T(t)/T_0]} , \quad (4.29)$$

where I_{tho} is the threshold current at the initial temperature, $I_{\text{th}}(t)$ is the threshold current at a time t later as the temperature changes according to Equation (3.1), and T_0 is the active region characteristic temperature ($\sim 150\text{K}$ for multi-quantum well diodes and $\sim 130\text{K}$ for single quantum well diodes^{2,4}). The threshold current increases with increasing temperature. For example, for $T_0=150\text{K}$ and $\Delta T = 5^\circ\text{K}$, $I_{\text{th}} = 1.034I_{\text{tho}}$. For $\Delta T = 10^\circ\text{K}$, $I_{\text{th}} = 1.069I_{\text{tho}}$.

The temperature dependence of the transparency electron current density, J_0 , and the differential gain coefficient, β , can be derived from the threshold current dependence using (4.15).³⁵ If the temperature dependence of J_0 is described by $J_0(\Delta T(t))=J_{0e}e^{[\Delta T(t)/T_0]}$ then $\beta(\Delta T(t))= \beta e^{[-\Delta T(t)/T_0]}$.

In this rate equation code, all the spectral shift is assumed to occur via mode hopping. This is because the individual modes are being modeled. The mode chirping can easily be predicted, though, knowing the average shift in the wavelength of the individual modes with temperature. It is important to

remember, though, when comparing the modeling to the experimental data, that if mode chirping is severe enough, the experimental data will not give an accurate measure of the mode hopping, because the mode will be moving out of the detector area during the pulse.

4.7 Refractive Indexes

The group refractive index, n_g , is defined as

$$n_g = n_r - \lambda \frac{dn_r}{d\lambda}, \quad (4.30)$$

where n_r is the effective refractive index of the material. The group refractive index was estimated for a GaAlAs SQW laser at an energy of 1.455 eV to be 3.87.⁵⁵ Larsson, et.al.,⁵⁶ report values for the group index as 3.45 to 3.8 for GRINSCH SQW lasers with cavity lengths ranging from 300 to 600 μm . This value concurs with values obtained from the measurements of the separation of the laser diode modes with a spectrometer and equation (4.24). These values are listed in Table 5.2 of Chapter 5 for several of the lasers tested in this report. The effective refractive index of the GaAs laser medium for laser energy at 1.5 eV is found to be near 3.65.¹²

4.8 Confinement factor

The confinement factor, Γ , is the fraction of the mode energy contained in the active region. It also is an approximate ratio of the electron volume in the active area to the volume occupied by the optical modes, and is defined as

$$\Gamma = \frac{\int_{-d/2}^{d/2} E_y^2 dx}{\int_{-\infty}^{\infty} E_y^2 dx} \quad (4.31)$$

where E_y is the electric field and d is the active area thickness.⁶ The confinement factor can be approximated by the use of the effective optical width, s ,

$$s = \frac{\int_{-\infty}^{\infty} E_y^2 dx}{E_{\max}^2} \quad (4.32)$$

where E_{\max} is the electric field at the center of the active area. The effective optical width is close to the full width/half maximum of the optical power profile. The confinement factor can then be approximated by

$$\Gamma \approx \frac{d}{s} \quad (4.33)$$

A simple relationship calculating Γ from the refractive indexes of the material, the active layer thickness, and the wavelength can be found in Agrawal and Dutta.³⁴ This relationship is an approximation assuming most of the power is in the fundamental transverse mode. The normalized waveguide thickness is now introduced:

$$D = k_0 (\mu_a^2 - \mu_c^2)^{.5} d \quad (4.34)$$

where μ_a and μ_c are the refractive indices of the active layer and the cladding layers, k_0 is the wave number of the mode,

$$k_0 = \frac{2\pi}{\lambda_0} \quad (4.35)$$

and λ_0 is the free space wavelength. The confinement factor can then be approximated as³⁴

$$\Gamma = D^2 / (2 + D^2) \quad (4.36)$$

for D in μm . For quantum well lasers, where $D \ll 1$, this equation can be further simplified to $\Gamma = D^2/2$ or

$$\Gamma = 2\pi^2 (\mu_a^2 - \mu_c^2) d^2 / \lambda_0^2. \quad (4.37)$$

Table I shows some calculations of the confinement factor and effective optical thicknesses for various refractive indexes, wavelengths, and active layer thicknesses.

Table 4.2
Calculated Confinement Factors and Effective Optical Thicknesses

$\lambda_0, \mu\text{m}$	$d, \mu\text{m}$	μ_a	μ_c	Γ	$s, \mu\text{m}$
0.8	1.0	3.51	3.22	0.98	1.02
0.8	0.1	3.51	3.22	0.376	.266
0.8	.06	3.51	3.22	.178	.337
0.8	.02	3.51	3.22	.0235	.851
0.8	.01	3.51	3.22	.006	1.67

Kressel and Butler¹² and Thompson⁶ get similar results as those shown in Table I. As can be seen, the effective optical thickness, s , increases dramatically for active layer sizes less than $0.1 \mu\text{m}$.

Quantum well structures allow high gain at low carrier densities but have the disadvantage of a small optical confinement factor.⁴⁷ Two means of combating this are the use of multi-quantum wells and a graded index confinement structure.

The optical confinement factor for graded-index structures must be calculated numerically. Wagner et.al.² calculates this for various laser lengths and widths. For a laser with a quantum well active layer thickness of 10 nm , the confinement factor was 0.032 , giving an effective optical thickness, s , of $0.312 \mu\text{m}$. This is a considerable improvement over the non-graded structure. For the $0.014 \mu\text{m}$ active layer thickness SQW GRIN SCH lasers used in this report, a confinement factor of 0.045 was used which gives the same effective optical thickness of $0.312 \mu\text{m}$.

Agrawal and Dutta³⁴ calculate the confinement factor for multi-quantum -well lasers as

$$\Gamma = \gamma \frac{N_a d_a}{N_a d_a + N_b d_b} \quad (4.38)$$

where

$$\gamma = 2 \pi^2 (N_a d_a + N_b d_b)^2 \frac{\bar{\mu}^2 - \mu_c^2}{\lambda_0^2},$$

$$\bar{\mu} = \frac{N_a d_a \mu_a + N_b d_b \mu_b}{N_a d_a + N_b d_b}.$$

and N_a and N_b are the number of active and barrier layers. Using these formulas Γ is calculated to be 0.147 for a $0.808 \mu\text{m}$ wavelength laser with four

active layers each 13 nm thick and three barrier layers each 4 nm thick. In this case s will be $0.436 \mu\text{m}$.

4.9 Cavity loss coefficient

The effect of the loss coefficient, α_i , in the rate equations is to change the overall output power of all the modes. Raising α_i will lower the output power. The main cavity loss mechanisms are free-carrier absorption in the quantum well and in the graded and confining layers. The intrinsic loss coefficient is related to these by the confinement factor,

$$\alpha_i = \alpha_{qw} \Gamma + \alpha_{cl} (1 - \Gamma). \quad (4.39)$$

The free carrier absorption coefficients in the quantum well and graded and confining layers, α_{qw} and α_{cl} , have values in the range of 30 cm^{-1} and 2 cm^{-1} . In Wagner, Waters, et.al.,² values for α_i are found for a SQW, GRINSCH structure laser. They obtain values from 2.8 to 5.5 cm^{-1} for different structures.

The external quantum efficiency, η_e , can be related to the internal quantum efficiency, η_i , by the equation:

$$\eta_e = \eta_i \frac{\ln(1/R)}{\alpha_i L + \ln(1/R)} \quad (4.40)$$

The internal quantum efficiency of these lasers is known to be near 1.0.¹² The differential quantum efficiency is the slope of the optical power versus injection current graph (in W/A) divided by the bandgap energy in eV where the bandgap energy in eV is equal to $1.24/\lambda_{po}$, with λ_{po} in microns.

4.10 Spontaneous Electron Lifetime

The carrier (or electron) lifetime, τ_e , is the carrier lifetime in the active region. It is the inverse of the carrier recombination rate and is defined by

$$\frac{1}{\tau_e} = A_{nr} + B n_e + C n_e^2 \quad (4.41)$$

where

A_{nr} = non-radiative recombination rate due to traps or surface recombination, s^{-1} ,

B = radiative recombination coefficient, cm^3/s ,

C = Auger recombination coefficient, cm^6/s .

The carrier lifetime is related to the carrier lifetime due to radiative recombination processes, τ_r , and the carrier lifetime due to nonradiative recombination processes, τ_{nr} , by,

$$\frac{1}{\tau_e} = \frac{1}{\tau_r} + \frac{1}{\tau_{nr}} \quad (4.42)$$

where $\frac{1}{\tau_r} = B n_e$ and $\frac{1}{\tau_{nr}} = A_{nr} + C n_e^2$.

Olshansky, et. al., have reported values for the A_{nr} , B , and C coefficients for AlGaAs LEDs and InGaAsP lasers.⁵⁷ They found that the Auger coefficient is negligible for AlGaAs LEDs. It should be noted that the carrier lifetime will remain a constant once threshold is reached because at that point and at higher current levels the electron density, n_e , remains a constant. The rate equation modeling in this report is designed to model lasers that are pulsed

from threshold and so a single value for the carrier lifetime at threshold can be used. If it was desired to model the lasers pulsed from zero current the A_{nr} and B coefficients would need to be used. The A_{nr} and B coefficients can be found by measurements of the carrier lifetime versus current as described by Olshansky. Since the A_{nr} coefficient is usually on the order of 5 to 10 times smaller than the Bn_e term at threshold, τ_r is approximately equal to τ_e and there is only a relatively small discrepancy if τ_e is used for τ_r in Equation (4.2) so that the equations can be normalized more easily.

The carrier lifetime for the MQW-4-250 laser can be found experimentally from the fall time of a pulse.¹² The diode was pulsed below threshold and the fall time measured. For this work a Berkeley Nucleonics Model 6040 Pulse Generator with a Model 201E Module with 150 ps rise and fall times was used to pulse the laser. An Antel Optronics Model AR-S5 APD with a <90 ps rise time was used to detect the signal. For the MQW-4-250 single-stripe laser the fall time was found to be approximately 1.2 ns.

The carrier lifetime can also be calculated from the expression¹¹

$$\tau_d = t_0 + \tau_e \ln[I/(I - I_{th})] , \quad (4.43)$$

where τ_d is the delay time between the onset of the current pulse and the output from the laser, and t_0 is a fixed arbitrary delay caused by cables. The pulse current is measured from an initially unbiased value. With this equation, if several values are taken and plotted, the electron lifetime can be found from the slope of the curve of (τ_d) versus $(\tau_e \ln[I/(I - I_{th})])$. Elliott, et.al.,¹¹ calculated the lifetime this way for the 10-stripe MQW-100-250 laser and found a value of 1.9 ns. Streifer, et.al., uses the value of 1.6 ns for a MQW laser at threshold.⁵⁸

Changing the carrier lifetime in the rate equations program changes the oscillation frequency. This is because it is directly related to the stimulated emission factor as shown in Equation (4.12). A larger value of τ_e decreases the number of oscillations per nanosecond.

4.11 Limitations of the rate equation model

Several factors limit the accuracy of our model.

Firstly, the gain/current relationship is assumed to be linear when in fact there are non-linearities present.

Secondly, the model does not take into account mode chirping. It assumes the modes stay at a constant wavelength and only the power distribution between modes changes.

Values for γ , τ_{sp} , Γ , and α are approximate and will vary even among lasers of the same type.

However, with all these inaccuracies, the rate equation model is still useful as a tool to obtain rough measurements of the behavior of pulsed laser diodes, particularly when various design parameters need to be compared.

A complete listing of the rate equation computer program in Mathematica for a MacIntosh computer is given in Appendix A.

CHAPTER 5

USING THE RATE EQUATION MODEL

5.1 Introduction

The rate equation model can be used with or without including thermal effects. Without thermal effects the model can be run to get information on relaxation oscillation frequency, modal power distribution, total output power, and the settling time of the modal power fluctuations due to mode buildup-time transients.

When temperature dependence is added, the relaxation oscillation frequency and total output power remain the same. The change is that now the peak of the gain curve will shift and the modes will shift in power accordingly. The longer wavelength modes will gain power and the shorter wavelength modes will lose power.

5.2 Modeling the laser diodes without incorporating thermal effects

Table 5.1 lists the input parameters for the lasers used in the simulations. Wavelength and spacing between the individual modes, $\Delta\lambda_c$, taken with an LS-2 spectrometer, are also presented. These were used to calculate values for the group index, n_g . A value of 1.8 ns^{-1} was used for τ_{sp} , $0.025 \text{ } \mu\text{m}$ for $\Delta\lambda_D$, and 0.3 and 0.95 for R1 and R2. Section 4.8 describes how the confinement factors, Γ , were obtained. Section 4.3 describes how the differential gain coefficient, β , and the transparency current density, J_0 , were obtained.

TABLE 5.1

Individual Input Parameters for the Laser Diodes

Parameter	SQW-60-300	SQW-60-600	SQW-5-300	MQW-4-250
D (μm)	60	60	5	4
L (μm)	300	600	300	250
d (μm)	0.014	0.014	0.014	0.064
Γ	0.045 ²	0.045 ²	0.045 ²	0.147
β (cm/A)	4.4	4.4	0.51	0.12
J_0 (A/cm ²)	145	145	225	565
n_r	3.65 ¹²	3.65 ¹²	3.65 ¹²	3.6
λ_{po} (μm)	0.814	0.822	0.819	0.80
I_{th} (mA)	100	100	75	49
Differential Quantum Efficiency	0.473	0.5	0.623	0.42
λ_{po} (μm) (from LS-2)	0.812	0.818	0.811	0.802
$\Delta\lambda_c$ (nm) (from LS-2)	0.312	0.137	0.305	0.30
n_g	3.52	3.96	3.59	4.3

Simulations of the modal transient response without thermal effects for four lasers were performed. Table 5.2 shows the results along with values obtained experimentally. The relative output power of the individual modes for the lasers was not determined experimentally but can be compared qualitatively from the experimental data presented in Figures 2.4 through 2.11.

TABLE 5.2

Rate Equation Program Results for the Laser Diodes

Parameter	Exper Value	Calc. Value	Exper Value	Calc. Value	Exper Value	Calc. Value	Exper Value	Calc. Value
Laser	SQW-60-300		SQW-60-600		SQW-5-300		MQW-4-250	
Current, mA	200		200		128		80	
Intrinsic Loss, α_i , cm^{-1}	29		14		39		60	
Astigmatism Factor, K	68		32		2.5		2	
Total Output Power, mW	80	83	65	68	46	46	20	19
Threshold Current, mA	100	74	100	99	75	44	49	38
Oscill. Frequency, ns^{-1}	3.2	4.0	2.4	2.4	1.7	3.8	2.7	3.3
Mode buildup time, center mode, ns	-10	10	-30	30	-10	15	-8	15
Output Power, mW:								
Mode 1	-	23	-	12	-	23	-	9
Mode 2	-	13	-	10	-	7	-	3.8
Mode 3	-	7	-	6	-	1.5	-	1
Mode 4	-	3	-	4	-	0.5	-	0.5

When the rate equation runs are being done, the gain parameters, carrier lifetime, and laser dimensions are entered into the program and then trial and error runs are made to fit the calculated results to the experimental data by adjusting the astigmatism factor and the intrinsic loss coefficient. The astigmatism factor (as part of the spontaneous emission factor, γ) affects the mode power distribution and to a small extent the oscillation frequency of the relaxation oscillations. A larger γ causes a larger spread of the power distribution of the modes and a slightly higher oscillation frequency. The spontaneous emission factor also affects the time it takes for the modal power sharing to settle, with a smaller γ causing the modes to take longer to stabilize in power. The effect of the loss coefficient, α_i , in the rate equations is to change the overall output power of all the modes. Raising α_i will lower the total output power. These values of the astigmatism factor and the intrinsic loss coefficient are only approximations, though, due to the approximate

nature of several of the other input parameters, such as the confinement factor, the electron lifetime, and the gain coefficients.

Close agreement is obtained between the experimental and calculated values for the SQW-60-300 laser for the total output power, the relaxation oscillation frequency, and the mode buildup time. Figure 5.1a shows the output from four of the dominant modes for the SQW-60-300 laser. This can be compared to the experimental data in Figure 2.4. Mode 0 is the center mode, and modes 1 through 3 are side modes which have identical counterparts on the other wavelength side of mode 0. The mode buildup-time represents the time it takes for the center mode to reach 86% (two time constants) of the final value. The other modes settle faster, at rates that are proportional to their distance from the center mode. Figure 5.1b shows the electron concentration as a function of time during the pulse. All the rate equation runs are started from a current slightly below threshold. As can be seen, the electron concentration rises to the threshold value and then oscillates around this value before leveling out.

Figure 5.2 shows the output from six of the dominant modes for the SQW-60-600 laser diode. A smaller astigmatism factor, K , for the spontaneous emission factor, γ , was needed for this laser to match the experimental data. The smaller γ needed for this laser is related to the fact that with the longer length, the allowed angular spread of the individual modes is less so that a smaller percentage of the spontaneous emission (which is emitted in all directions) will go into the lasing modes.

The mode buildup-time for the SQW-60-600 laser is considerably longer than for the SQW-60-300 laser. This is related to the fact that it has a smaller spontaneous emission factor and also to the fact that the photon lifetime for this laser will be longer because of the longer length and so the competition

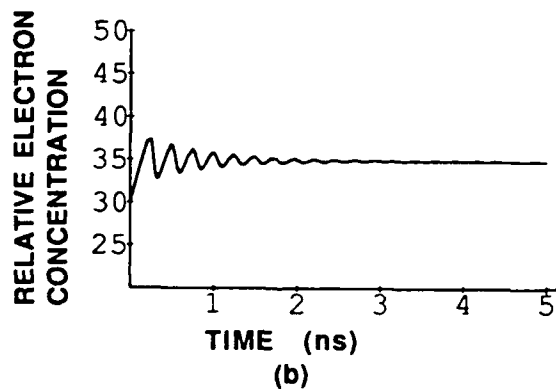
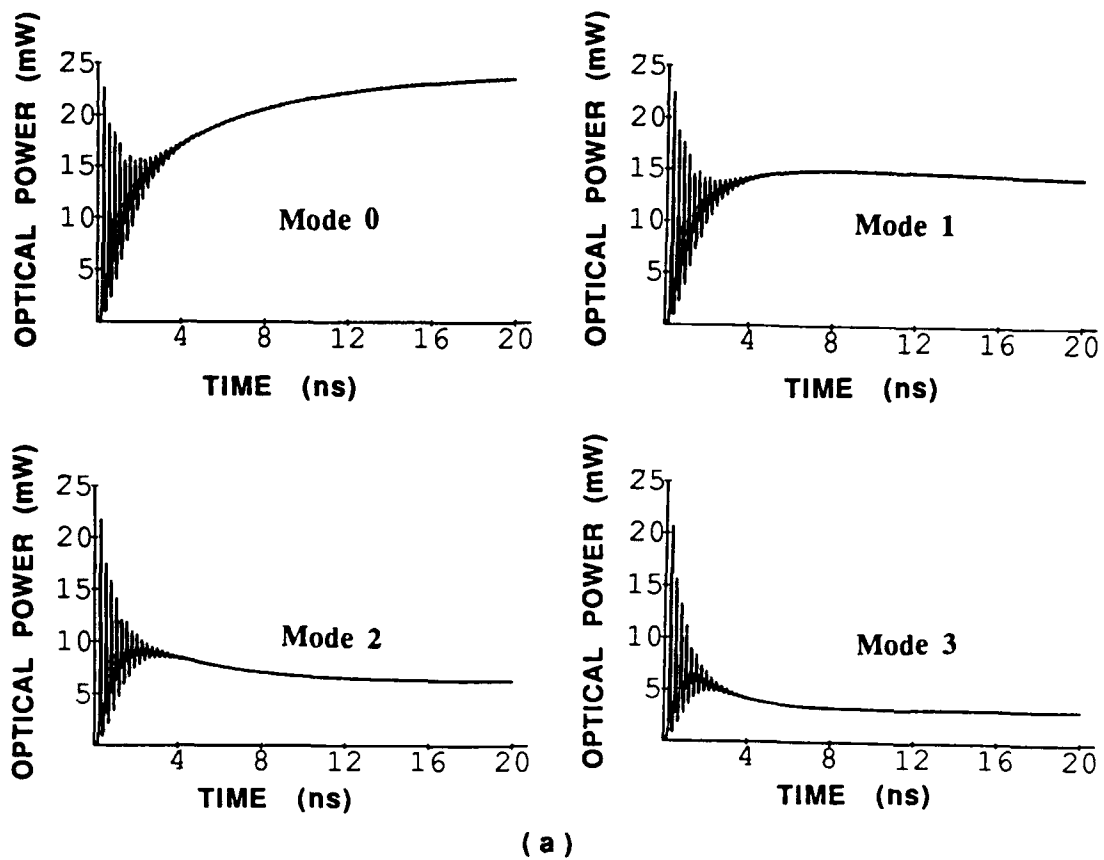


FIGURE 5.1 Rate equation modeling for the SQW-60-300 laser diode showing (a) output power; and (b) relative electron concentration; from four lasing modes.

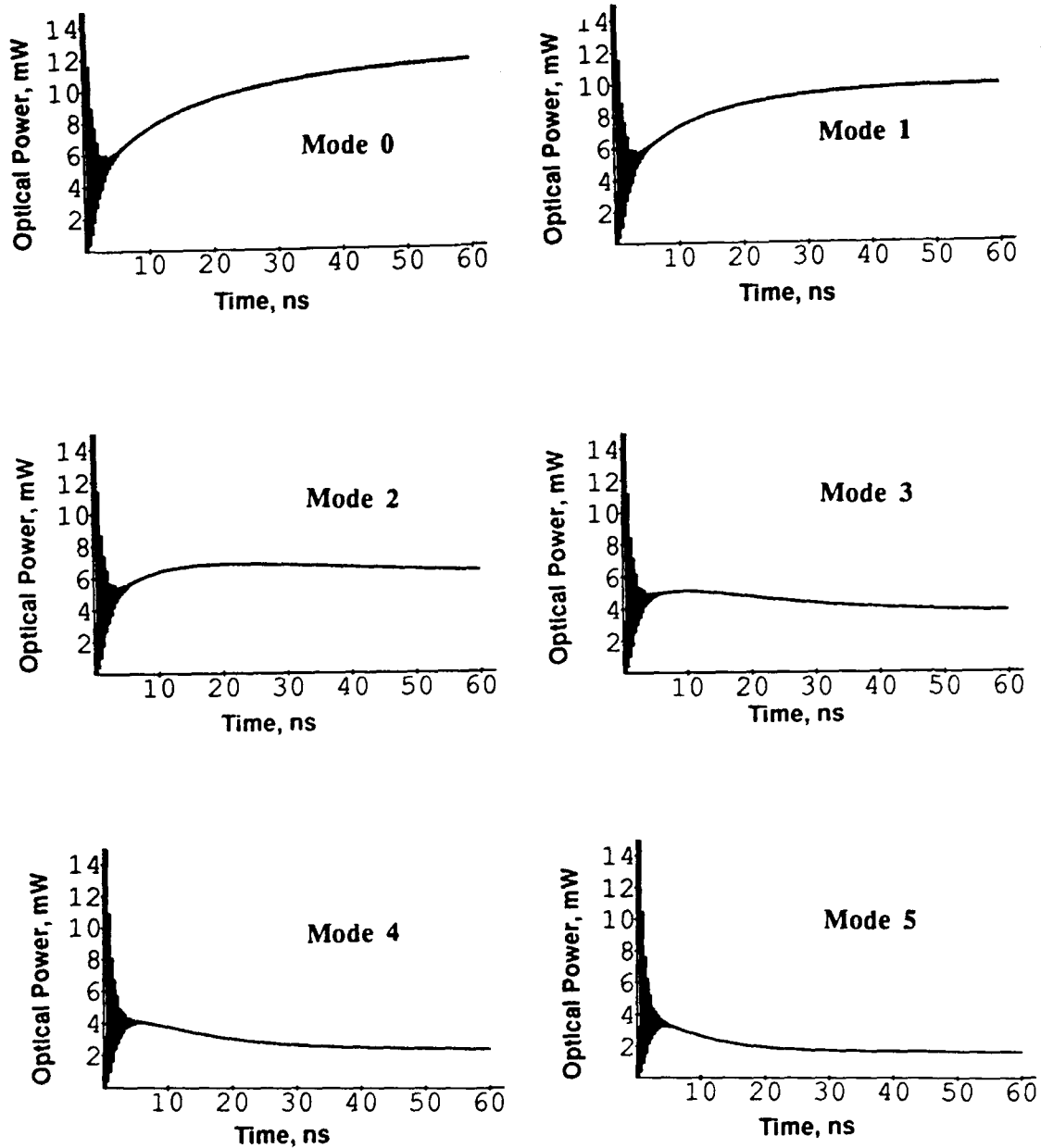


FIGURE 5.2 Rate equation modeling for the SQW-60-600 laser diode showing output from six lasing modes.

between the modes takes longer to resolve. The mode spacing for this laser is half that of the SQW-60-300 laser and the output power is spread out more between the modes.

Figure 5.3 shows the output from the four dominant modes for the SQW-5-300 laser diode using the effective values of β and J_0 of 0.51 cm/A and 225 A/cm² calculated using a diffusion length of 5 μm and current spreading length of 1.2 μm . The total output power and mode buildup time matched the experimental data well, however, the calculated oscillation frequency for this laser of 3.8 GHz did not match the experimental value of 1.7 GHz well. This indicates that either the effective value of β is too high or that the carrier lifetime, τ_e , is too low. Using effective values of β and J_0 of 0.32 and 375, determined from the current spreading calculation with a diffusion length of 8 μm and current spreading length of 5 μm , a value of 2.6 GHz was obtained for the oscillation frequency. With these longer diffusion and current spreading lengths, a calculated current threshold of 66 mA was obtained which is closer to the experimental value of 75 mA than the value of 44 mA obtained using the calculated diffusion and current spreading lengths. Using these longer diffusion and current spreading lengths is not reasonable, however, since the experimental data taken by imaging the laser facet below threshold does not indicate that there is that much spread in the current profile. It is apparent that some other factor, such as a change in the carrier lifetime, is playing a role in the behavior of these narrow stripe lasers.

The SQW-5-300 laser needed a much smaller astigmatism factor, K , of 2.5 to match the steady state distribution of power between the modes. This is due to the fact that since it is a narrow stripe, the allowed angular spread of the individual modes is less than for a broad stripe laser and a smaller percentage

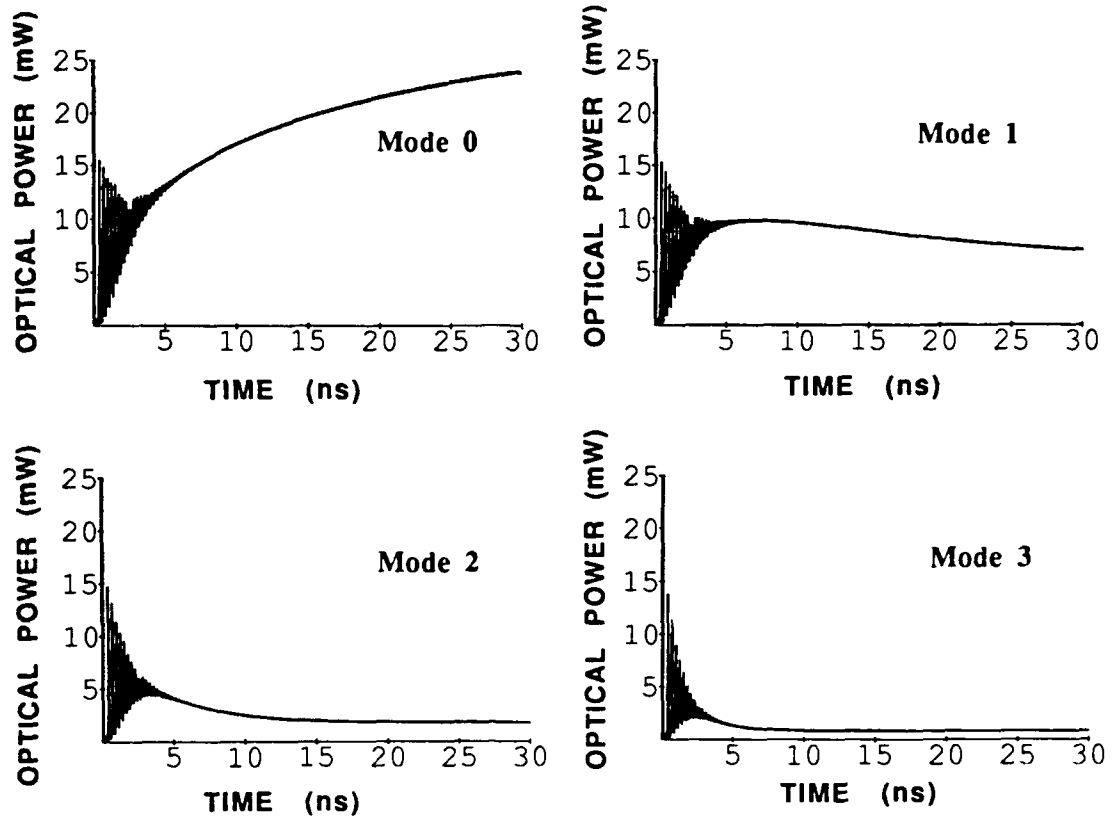


FIGURE 5.3 Rate equation modeling for the SQW-5-300 laser diode showing output from four lasing modes.

of the spontaneous emission (which is emitted in all directions) will go into the allowed lasing modes.

Table 5.1 also lists the input parameters used to model the MQW-4-250 narrow stripe laser diode. A MQW laser typically consists of four $0.013 \mu\text{m}$ thick layers of $\text{Ga}_{0.94}\text{Al}_{0.06}\text{As}$ separated by three $0.004 \mu\text{m}$ thick layers of $\text{Ga}_{0.8}\text{Al}_{0.2}\text{As}$.¹⁸ An effective thickness of $0.064 \mu\text{m}$ and confinement factor of 0.147 were used to model this laser.

The experimental relaxation oscillations from the MQW-4-250 laser were determined in a paper by Elliott and DeFreez.¹¹ The relaxation oscillations had a frequency of 1.7 GHz (1.7 oscillations/ns) for a current 1.3 times the threshold current and 4.0 GHz (4 oscillations/ns) for a current twice threshold. This data can be extrapolated for a current 1.6 times threshold to give 2.7 oscillations/ns.

The rate equation results for the MQW-4-250 are presented in Table 5.2. Effective values of β and J_0 of 0.2 and 750 were found to give results close to those found experimentally. (Intrinsic values of β and J_0 could not be found for this laser.) Figure 5.4 shows the output from the four dominant modes. The value of 2.0 for K needed for this laser is close to the value of 3 calculated in a report by Hausser, et. al.,⁵³ for narrow stripe MQW lasers.

All the runs were done using 19 modes in the calculation. When only 9 modes were used the results were similar. With 9 modes the oscillations were more prominent but the modes settled to approximately the same powers and the average power was approximately the same.

A run was also done for the SQW-60-300 laser with the gain curve peaked between two modes. In this case the results are very similar except for the fact that there are now two identical center modes with slightly less power

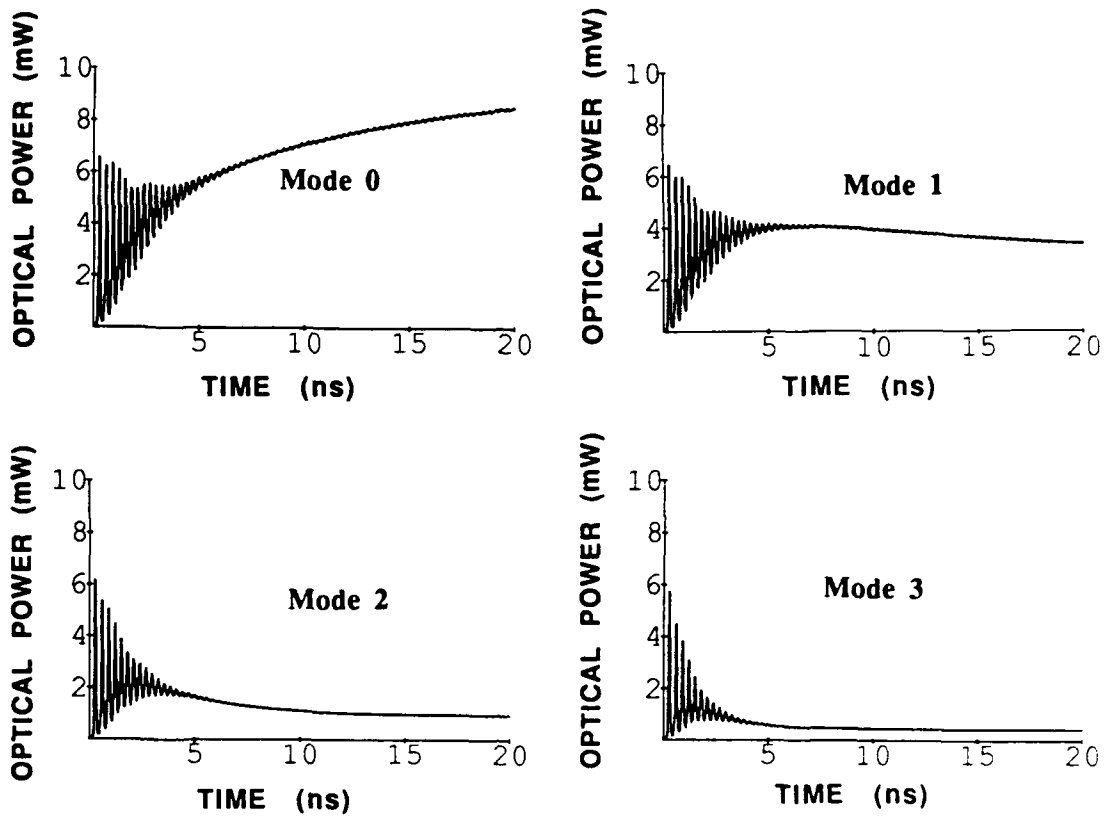


FIGURE 5.4 Rate equation modeling for the MQW-4-250 laser diode with 20 mW output power and a 20 ns pulse.

than the one center mode for the case of the gain peak centered on one mode. The settling times (or mode buildup time) for the modes remained approximately the same.

Although the gain saturation factor, ϵ , was not used in the rate equation runs, values for ϵ could be obtained by trial and error that damp out the oscillations in about two nanoseconds. A value of $2.0 \times 10^{-6} \mu\text{m}^3$ was obtained for the SQW-5-300 laser, $24 \times 10^{-6} \mu\text{m}^3$ for the SQW-60-300 and the SQW-60-600 lasers, and $3.5 \times 10^{-6} \mu\text{m}^3$ for the MQW-4-250 laser.

5.3 Modeling the laser diodes with thermal effects

As stated earlier, when temperature dependence is added to the rate equation modeling, the relaxation oscillation frequency and total output power remain the same. The change is that now the peak of the gain curve will shift with time and the modes will shift in power accordingly. The longer wavelength modes will gain power, and the shorter wavelength modes will lose power.

Table 3-8 lists the thermal time constants for the SQW-60-300 and SQW-5-300 lasers derived from the finite element analysis. The parameters k_1 , k_2 , T_1 , and T_2 are dependent on how much drive current is applied to the diode and so must be determined for a specific value of current.

The characteristic temperature used was 125°K^2 . A value of $0.25 \text{ nm}/^\circ\text{K}$ was used for h .

Figures 5.5 and 5.6 show the rate equation modeling with thermal effects for the SQW-60-300 laser for 80 mW power output (100 mA modulation current) and 80 ns and 1000 ns pulses using the finite element analysis derived thermal parameters. These can be compared to the experimental data

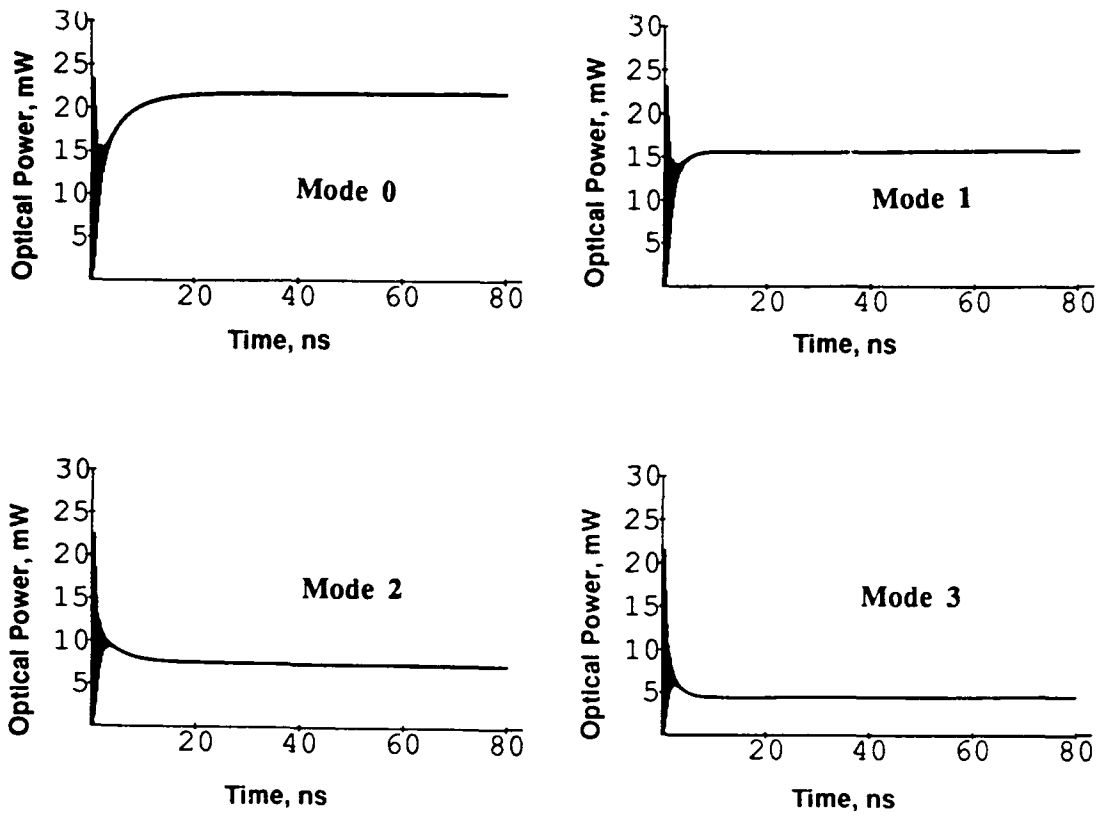


FIGURE 5.5 Rate equation modeling for the SQW-60-300 laser with thermal effects derived from the finite element analysis for 80 mW output power and an 80 ns pulse.

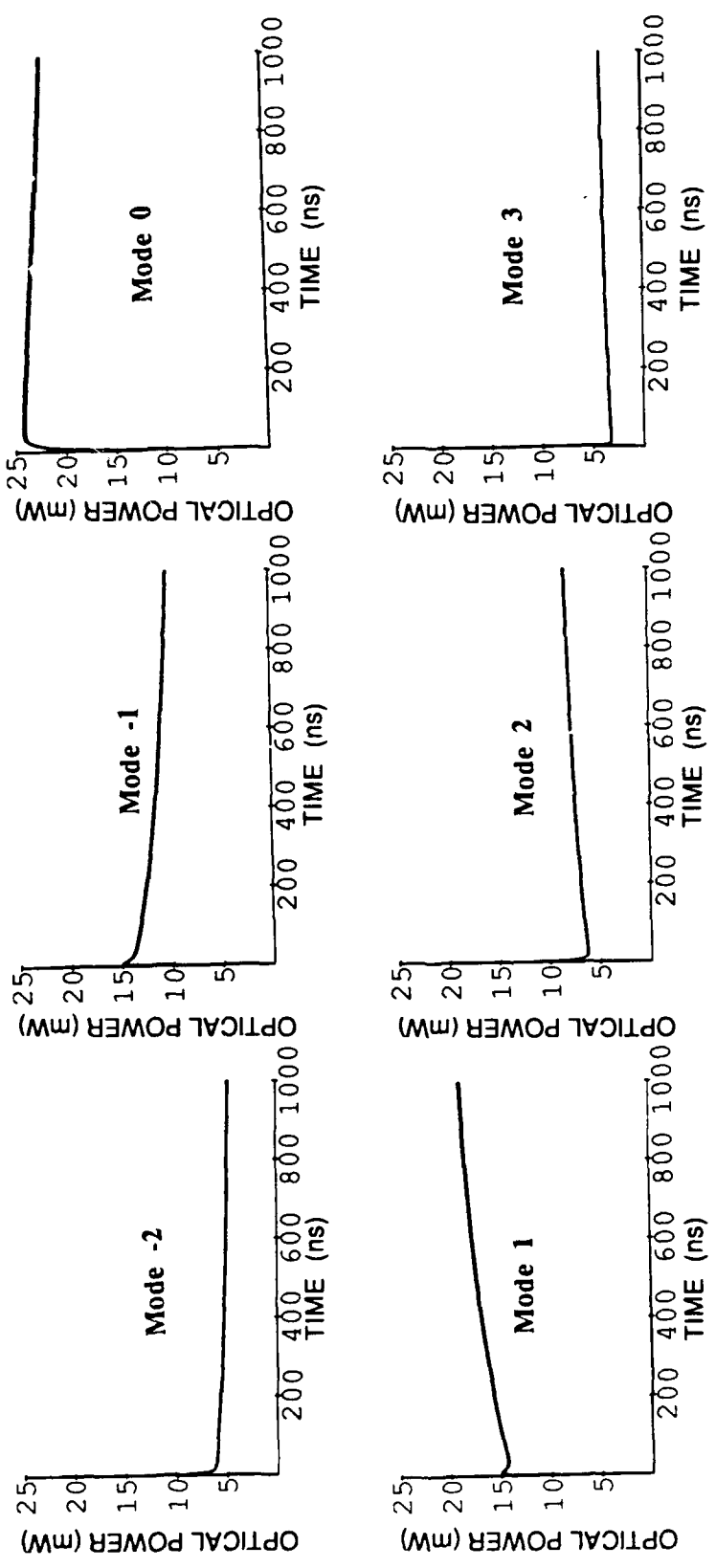


FIGURE 5.6 Rate equation modeling for the SQW-60-300 laser with thermal parameters derived from the finite element analysis for 80 mW output power and a 1000 ns pulse.

in Figures 2.4 and 2.5. This laser had fairly small thermal fluxes for the 80 mW power level and this is confirmed by the modeling. The thermal transients for the 80 ns pulse are too small to be detected. Small thermal transients of the same magnitude are observable, though, for the 1000 ns pulse in the modeling and the experimental data.

Figure 5.7 shows the rate equation modeling for the SQW-5-300 laser for 46 mW power output and an 80 ns pulse using the finite element analysis derived thermal parameters with a FWHM of 5 μm for the current profile. As can be seen by comparing this data to the experimental data in Figure 2.8, the experimental thermal transients are reasonably close to the calculated ones. Figure 5.8 shows the SQW-5-300 laser modeled with 46 mW optical power output and a 1000 ns pulse. Once again, the experimental thermal transients look reasonably close to the calculated ones, though, a direct comparison cannot be made to the experimental data of Figure 2.9 because, as stated earlier, the transients for this laser are of a high enough magnitude to cause the modes to shift through the detector area during the pulse, making the degree of mode hopping appear larger.

5.4 General discussion of rate equation modeling results

The rate equation results agree with the experimental data in describing the two types of transients occurring in these gain-guided lasers. Mode-buildup transients are more severe and occur at the beginning of the pulse. Their duration is dependent on the laser length, with 15 ns transients occurring in 300 μm length lasers, and 30 ns transients occurring in 600 μm length lasers.

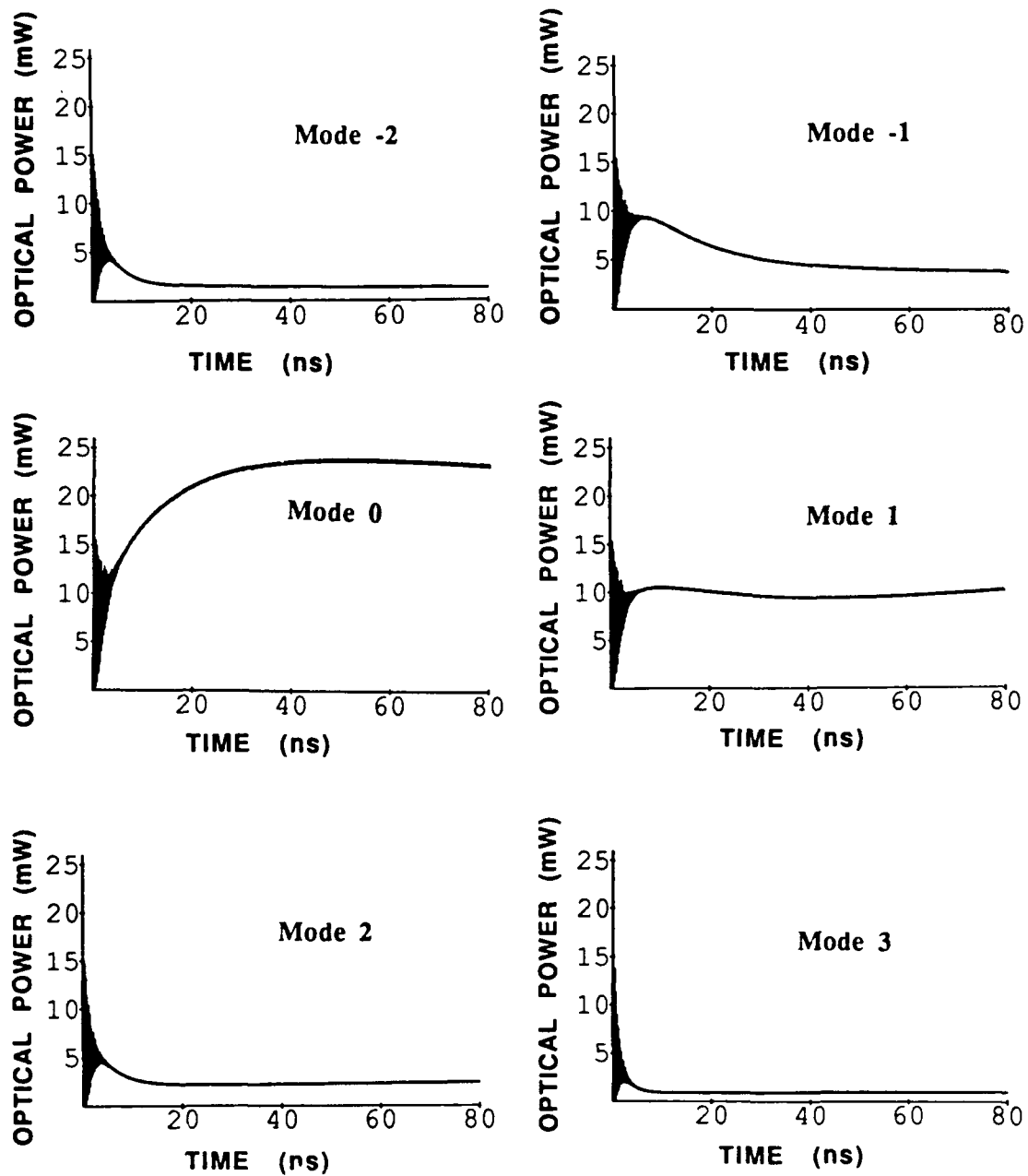


FIGURE 5.7 Rate equation modeling for the SQW-5-300 laser with thermal parameters derived from the finite element analysis for 46 mW output power, an 80 ns pulse, and a FWHM of 5 μm for the current profile.

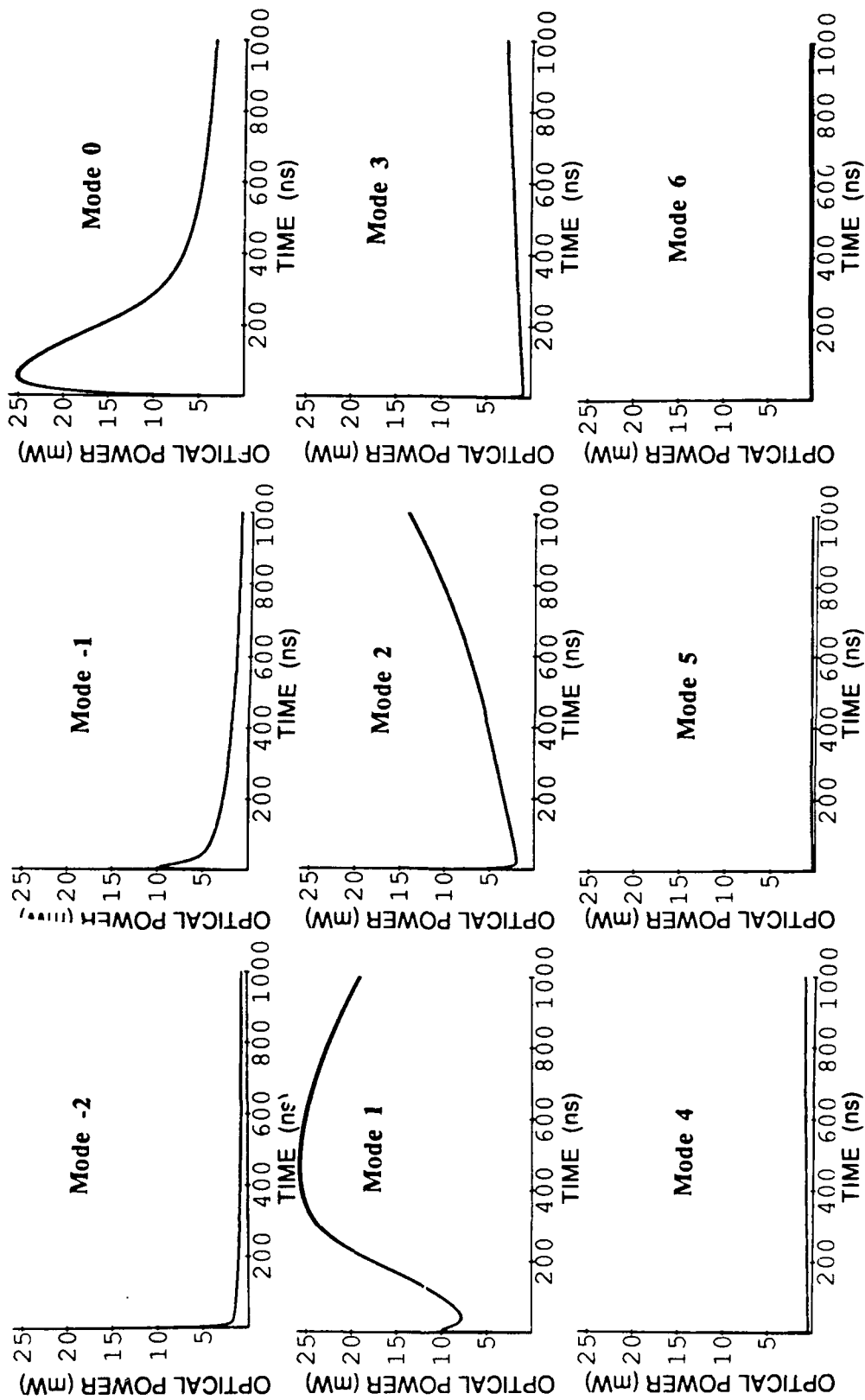


FIGURE 5.8 Rate equation modeling for the SQW-5-300 laser with thermal parameters derived from the finite element analysis for 46 mW output power, a 1000 ns pulse, and a FWHM of 5 μm for the current profile.

The rate equation program was found to give a good match to the experimental data for the broad stripe lasers. The minor discrepancies can be attributed to the inherent inaccuracy of some of the simplifying assumptions and the approximate nature of several of the input parameters. The thermal transients obtained from the rate equation analysis matched the experimental data well. The magnitude of the calculated thermal transients are dependent not only on the finite element analysis derived time constants, but also on the spontaneous emission factor. The spontaneous emission factor has a direct effect on the relative power distribution between the modes. If the power is spread more evenly between several modes (using a larger spontaneous emission factor), then the magnitude of the thermal transients will be less because a shift in the gain peak does not cause as great a shift in the magnitude of the modes.

For the narrow stripe lasers the match of the experimental data to the calculated data was not as good. Longer diffusion and current spreading lengths than those calculated were needed to adjust the gain parameters to match the experimental relaxation oscillation frequency and threshold current. However, these longer lengths were not confirmed by experimental data taken by imaging the laser facet below threshold. The experimental data indicated that the current profile narrows considerably near threshold. A reasonable match of the experimental and calculated thermal transients was obtained by using a FWHM of 5 μm for the current profile. Modeling of narrow stripe lasers is an area for further investigation.

CHAPTER 6

CONCLUSIONS

In this report the axial mode instabilities for several laser diode structures were examined. In Chapter 2, experimental data was taken and the general results showed two types of modal transients present. Mode buildup transients occur over a relatively short period of time (10-60 ns) that is dependent on the photon lifetime (and consequently laser length, with shorter lengths having smaller transients). Thermal transients occur over a period of several hundred nanoseconds.

The broad-stripe GRINSCH SQW laser diodes had negligible thermal transients for the peak modulation depth of 100 mA. The MQW narrow stripe laser and SQW narrow-stripe laser had large thermal transients.

In Chapter 3, the steady state temperature increase of the laser diodes and the temperature changes in the active area during a current pulse were modeled with a finite element code. A detailed analysis of the laser was done 2-dimensionally, with a 3-dimensional analysis performed to determine the thermal impedance of the heat sink.

In Chapter 4, the thermal modeling was combined with rate equations to give a complete model of how the laser modes behave during modulation. The rate equation model without thermal effects gave information on relaxation oscillation frequency, threshold current, modal power distribution, total output power, and the settling time of the modes due to mode buildup transients. Adding thermal effects shifted the power distribution of the modes according to the entered thermal time constants in a very predictable fashion.

The rate equation results agreed with the experimental data in describing the two types of transients occurring in these gain-guided lasers.

Mode buildup-time transients are more severe and occur at the beginning of the pulse. Their duration is dependent on the laser lengths, with 10-30 ns transients occurring in 300 μm length lasers, and 20-60 ns transients occurring in 600 μm length lasers. The rate equation program was found to give a good match to the experimental data for the broad stripe lasers. The minor discrepancies can be attributed to the inherent inaccuracy of some of the simplifying assumptions and the approximate nature of several of the input parameters. Using the rate equation model with the finite element code derived thermal parameters was found to give a good match to the experimental data.

A method was found to solve for the gain constant and the transparency current density for narrow-stripe lasers. Current spreading in the narrow-stripe lasers was found to have a large effect on these constants. Diffusion and current spreading lengths longer than those calculated, however, were necessary to match the experimental data on the relaxation oscillation frequency and the threshold current. This was not consistent with the thermal modeling and the experimental data taken by imaging the laser facet, which indicates that the current spreading region should be less than that calculated. A good match to experimental thermal transients, however, was obtained using the thermal modeling with the rate equations.

Further works needs to be done on modeling the narrow stripe lasers, however, it should be noted that these laterally gain-guided narrow stripe lasers are not used as frequently nowadays, because index-guided or buried heterostructure lasers, which have lateral current confinement, are more commonly available and are preferred over gain-guided devices particularly for communication purposes.

A broad-stripe GRIN SCH SQW laser diode with a 200-250 μm length would be a good structure for minimizing both mode buildup-time transients and thermally-induced transients. This type of structure could output 100 mW of output power with minimal modal instability. Going to higher output powers could still be a problem, though, since the thermal transients are directly related to modulation depth.

REFERENCES

- [1] W. Streifer, R. D. Burnham, T. L. Paoli, D. R. Scifres, "Phased Array Diode Lasers", *Laser Focus*, 100-109, June (1984).
- [2] D. K. Wagner, R. G. Waters, P. L. Tihanyi, D. S. Hill, A. J. Roza, Jr., H. J. Vollmer, M. M. Leopold, "Operating characteristics of single-quantum-well AlGaAs/GaAs high-power lasers", *IEEE J. of Quantum Electronics*, Vol. 24, No. 7, pp.1258-1265, July 1988.
- [3] R. G. Waters, P. L. Tihanyi, D. S. Hill, B. A. Soltz, "Progress in Single Quantum Well Structures for High Power Laser Device Applications", *SPIE Vol 893 High Power Laser Diodes and Applications*, pp. 203-209 (1988).
- [4] *Laser Diode Operator's Manual & Technical Notes*, Spectra Diode Labs, San Jose, CA, (1988).
- [5] S. E. Miller, D. Marcuse, "On fluctuation and transients in injection lasers", *IEEE J. Quantum Electronics*, Vol. QE-20, No. 9, 1032-1044 (1984).
- [6] G. H. B. Thompson, *Physics of Semiconductor Laser Devices*, John Wiley & Sons, New York (1980), Appendix 1.
- [7] M. Dagenais, Z. Pan, T. Ding, H. Lin, "Diode laser based optical logic devices", *Digital Optical Computing*, *SPIE Critical Reviews of Optical Science & Technology*, ed. R. A. Athale, SPIE Optical Engineering Press, Vol. CR35, pp. 126-154 (1990).
- [8] G. R. Gray, R. Roy, "Bistability and mode hopping in a semiconductor laser", *J. Opt. Soc. Am. B*, Vol 8, No. 3, 632-638 (1991).
- [9] Y. Nagai, K. Shigihara, A. Takami, S. Karakida, Y. Kokubo, A. Tada, "High-power operation of AlGaAs SQW-SCH broad-area laser diodes for Nd:YAG solid-state laser pumping", *IEEE Photonics Technology Letters*, Vol. 3, No. 2, 97-99, (1991).
- [10] N. Yu, R. K. DeFreez, D. J. Bossert, G. A. Wilson, R. A. Elliot, S. Wang, H. G. Winful, "Spatiospectral and picosecond spatiotemporal properties of a broad area operating channeled-substrate-planar laser array", *App. Opt.*, Vol. 30, No. 18, 2503-2513 (1991).
- [11] R.A. Elliott, R.K. De Freez, T.L. Paoli, R.D. Burnham, W. Streifer, "Dynamic characteristics of phase-locked multiple quantum well injection lasers", *IEEE J. of Quantum Electronics*, Vol. QE-21, No. 6, pp. 598-602, June 1985.
- [12] H. Kressel, J. K. Butler, *Semiconductor Lasers and Heterojunction LEDs*, Academic Press, New York (1977), pp. 416-433.
- [13] T. Yamamoto, K. Sakai, S. Akiba, Y. Itaya, Y. Suematsu, "Carrier lifetime measurement of InGaAsP/In P Double Heterostructure Lasers", *IOOC*, pp. 205-208. 1977.

- [14] *MSC/NASTRAN - Handbook for Thermal Analysis*, W. H. Booth, ed., MacNeal-Schwendler Corp., Los Angeles, Cal., 1986.
- [15] W. L. Lippincott, A. E. Clement, "Finite element analysis of thermal transients in multi-stripe laser diode arrays", SPIE Vol. 1045, Modeling and Simulation of Laser Systems, pp. 196-208 (1989).
- [16] W.L. Lippincott, A.E. Clement, W.C. Collins, "Experimental measurements of modal transients and theoretical thermal modeling of laser diodes", SPIE Vol. 1219, Laser Diode Technology and Applications II, pp. (1990).
- [17] N. Holonyak, R. M. Kolbas, R. D. Dupuis, P. D. Dapkus, "Quantum-Well Heterostructure Lasers", IEEE J. of Quantum Electronics, Vol. QE-16, No. 2, 170-186 (1980).
- [18] D.R. Scifres, R. D. Burnham, W. Streifer, "High power coupled multiple stripe quantum well injection lasers", Appl. Phys. Lett. 41(2), 118-120 (1982).
- [19] R. D. Burnham, W. Streifer, T. L. Paoli, "Growth and Characterization of AlGaAs/GaAs Quantum Well Lasers", J. of Crystal Growth 68, 370-382 (1984).
- [20] D. R. Scifres, W. Streifer, R. D. Burnham, "Experimental and Analytic Studies of Coupled Multiple Stripe Diode Lasers", IEEE J. of Quantum Electr., Vol. QE-15, No. 9, 917-922 (1979).
- [21] D. R. Scifres, R. D. Burnham, W. Streifer, M. Bernstein, "Lateral beam collimation of a phased array semiconductor laser", Appl. Phys. Lett., 41(7), 614-616 (1982).
- [22] J. S. Manning, "Thermal impedance of diode lasers: Comparison of experimental methods and a theoretical model", J. Appl. Physics, Vol. 52, No. 5, 3179-3184 (1981).
- [23] *Handbook of Chemistry and Physics*, 64th edition, Weast, R. C., ed., CRC Press, Inc. Boca Raton, FL. (1984).
- [24] *Chemical Engineers Handbook*, 5th ed., Perry, R. H., Chilton, C. H., ed., McGraw-Hill, N.Y. (1973).
- [25] *Langes' Handbook of Chemistry*, John A. Dean, ed., 13th edition, McGraw Hill, New York (1985).
- [26] M. A. Fromowitz, J. Appl. Phys. 44, 1292, (1973).
- [27] W. Engeler, M. Garfinkel, "Thermal Characteristics of GaAs Laser Junctions Under High Power Pulsed Conditions", Solid-State Electronics, Vol. 8, 585-604 (1965).
- [28] T. Yao, "Thermal properties of AlAs/GaAs Superlattices", Appl. Phys. Lett. 51(22), 1798-1800(1987).

- [29] M. Ito, T. Kimura, "Stationary and Transient Thermal Properties of Semiconductor Laser Diodes", IEEE J. Quantum Electronics, Vol. QE-17, No. 5, 787-795 (1981).
- [30] T. Kobayashi, Y. Furukawa, "Temperature Distributions in the GaAs-AlGaAs Double-Heterostructure Laser below and above the Threshold Current", Japanese J. of Appl. Physics, Vol. 14, No. 12, 1981-1986 (1975).
- [31] D. Marcuse, T. Lee, "On approximate analytical solutions of rate equations for studying transient spectra of injection lasers", IEEE J. Quantum Electron., vol. QE-19, pp. 1397-1406, 1983.
- [32] A. Yariv, *Quantum Electronics, Third Edition*, John Wiley & Sons, New York, 1989.
- [33] M.J. Adams, M. Osinski, "Longitudinal mode competition in semiconductor lasers - Rate equations revisited", IEE Proc. Vol. 129, Pt. I, No. 6, pp. 271-274, 1982.
- [34] J. P. Agrawal, N.K. Dutta, *Long-Wavelength Semiconductor Lasers*, Van Nostrand Reinhold Company, New York, 1986.
- [35] D.M. Byrne, B.A. Keating, "A laser diode model based on temperature dependent rate equations", IEEE Photonics Tech. Letters, Vol. 1, No. 11, pp. 356-359, 1989.
- [36] J. Manning, R. Olshansky, D. M. Fye, W. Powazinik, "Strong influence of nonlinear gain on spectral and dynamic characteristics on InGaAsP Lasers", Elect. Lett., Vol. 21, No. 11, 496-497 (1985).
- [37] C. B. Su, V. Lanzisera, R. Olshansky, "Measurement of nonlinear gain from FM modulation index of InGaAsP", Elect. Lett., Vol. 21, No. 11, 893-895 (1985).
- [38] D. Welford, S. B. Alexander, "Magnitude and phase characteristics of frequency modulation in directly modulated GaAlAs semiconductor diode lasers", J. Lightwave Tech., Vol. LT-3, No. 5, 1092-1099 (1985).
- [39] R. S. Tucker, D. J. Pope, "Circuit modeling of the effect of diffusion on damping in a narrow-stripe semiconductor laser". IEEE J. Quantum Electronics, Vol. QE-19, No. 7, 1179-1183 (1983).
- [40] H. C. Casey, Jr., M. B. Panish, *Heterostructure Lasers, Part B, Materials and Operating Characteristics*, Academic Press, New York (1978).
- [41] H. Yonezu, I. Sakuma, K. Kobayashi, T. Kamejima, M Ueno, Y. Nannichi, Jpn. J. Appl. Phys. Vol. 12, pp. 1585 (1973).
- [42] B. W. Hakki, "Striped GaAs lasers: Mode size and efficiency", J. Appl. Phys., Vol. 46, No. 6, 2723-2730 (1975).
- [43] W. Streiffer, R. D. Burnham, D. R. Scifres, "An analytic study of (GaAl)As gain guided lasers at threshold", IEEE J. Quantum Electronics, Vol. QE-18, No. 5, 856-864 (1982).

- [44] T. P. Lee, A. G. Dentai, "Power and modulation bandwidth of GaAs-AlGaAs high-radiance LED's for optical communication systems", IEEE J. Quantum Electronics, Vol. QE-14, No. 3, 150-159 (1978).
- [45] W. T. Tsang, "The effects of lateral current spreading, carrier out-diffusion, and optical mode losses on the threshold current density of GaAs-Al_xGa_{1-x}As stripe-geometry DH lasers", J. Appl. Phys. Vol 49, No. 3, 1031-1044 (1978).
- [46] J. Gowar, *Optical Communication Systems*, Prentice-Hall International, 1984.
- [47] R. Eppenga, M.F.H. Schuurmans, "Theory of the GaAs/AlGaAs quantum well", Philips Technical Review, Vol 44, No. 5, pp. 137-149, Nov. 1988.
- [48] P. Blood, S. Colak, A. I. Kucharska, "Influence of Broadening and High-Injection Effects on GaAs-AlGaAs Quantum Well Lasers", IEEE J. Q.E., Vol. 24, No. 8, pp. 1593-1604, August 1988.
- [49] D.V. Korbutyak, Y.V.Kryuchenko, V.G. Litovchenko, "Investigation of the optical gain spectra in two-dimensional quantum well heterostructures", Sov.Phys. JETP 69⁴, pp. 757-760, Oct. 1989.
- [50] M. Krahl, J. Christen, D. Bimberg, D. Mars, J. Miller, "Impact of Well Coupling on the spontaneous emission properties of GaAs/AlGaAs Multiple-quantum-well structures", IEEE J. of Q.E., Vol. 25, No.11, pp. 2281-2288, 1989.
- [51] K. Petermann, "Calculated spontaneous emission factor for double-heterostructure injection lasers with gain-induced waveguiding", IEEE J. Quantum Electronics, Vol. QE-15, No. 7, 566-570 (1979).
- [52] D. Marcuse, "Computer model of an injection laser amplifier", IEEE J. Quantum Electron., Vol. QE-19, No. 1, pp. 63-73, Jan. 1983.
- [53] S. Hausser, W. Idler, E. Zielinski, M. H. Pilkuhn, G. Weimann, W. Schlapp, "Spontaneous emission factor and waveguiding in GaAs/AlGaAs MQW lasers", IEEE J. Quantum Electronics, Vol. QE-25, No. 6, 1469-1476 (1989).
- [54] J. Manning, R. Olshansky, C.B.Su, "The Carrier-Induced Index Change in AlGaAs and 1.3 μm InGaAsP Diode Lasers", IEEE J. of Quantum Electronics, Vol. QE-19, No. 10, pp 1525-1530, Oct. 1983.
- [55] M.P. Kesler, C. Harder, "Gain and index measurements in GaAlAs Quantum Well Lasers", IEEE Photonics Technology Letters, Vol. 2, No. 7, pp. 464-466, 1990.
- [56] A. Larsson, P. A. Andrekson, B. Jonsson, C. Lindstrom, "Highly coherent long cavity GaAs/AlGaAs single-quantum-well lasers", IEEE J. Quantum Electronics, Vol. 25, No. 9, 2013-2018 (1989).

- [57] R. Olshansky, C.B. Su, J. Manning, W. Powazinik, "Measurement of radiative and nonradiative recombination rates in InGaAsP and AlGaAs light sources", IEEE J. Quantum Electronics, Vol. QE-20, No. 8, 838-854 (1984).
- [58] W. Streifer, D. F. Welch, J. Berger, D. R. Scifres, "Nonlinear analysis of Y-junction laser arrays", IEEE J. Q.E., Vol. 25, No. 7, pp. 1617-1624, 1989.

APPENDIX A

Computer Listing

```

<GrangeRutta.m
(* This program solves the rate equations for modal transients in laser diodes*)
(* It incorporates temperature effects into the rate equations *)

(* The set of units are microns, ns, coulombs, deg.K *)

(* CURRENT LEVELS *)

jth=.1 10^-9 (* threshold current into laser*)
(* (at 300 deg.K), A*10^-9 (C/ns) *)
current=.2 10^-9 (* current into laser, A*10^-9 (C/ns) *)

(* LASER DIMENSIONAL PARAMETERS *)
dthickness=.014 (* thickness of active laser region, microns*)
width=60 (* width of laser stripe, microns *)
L=300 (* cavity length, microns *)
refl=.3 (* reflectivity of first cavity mirror *)
refl2=.95 (* reflectivity of second cavity mirror *)
eta=.045 (* confinement factor*)
ng=3.52 (* group index of laser medium *)
nr=3.65 (* refractive index of laser medium *)

(* MISCELLANEOUS PARAMETERS *)

K=68 (* astigmatism factor used as multiplication factor for gamma *)
(* making gamma larger increases spread of power *)
(* and oscillations settle out faster *)
beta2p=4.4 10^-4 10^-9 (* gain constant, microns/(C/ns) *)
(* making gain constant larger increases oscill./ns.*)
(* and gives smaller time step *)
trans=145 10^-8 10^-9 (* transparency electron current density, (C/ns)/micron^2 *)
tsp=1.8 (* spontaneous emission lifetime, ns *)
alphao=29 10^-4 (* loss coefficient, microns^-1 *)
eps=0 12 2 10^-6 (* gain suppression factor, microns^3 *)
timestart=0 (* start of simulation, ns *)
timeend=20 (* end of simulation, ns *)
noticks=4 (* number of ticks on graph *)
estpower=40 (* estimated optical power out, this scales the printout, mW*)

c=3 10^5 (* velocity of light, microns per ns *)
co=3 10^14 (* velocity of light, microns per sec *)
ee=1.6 10^-19 (* electron charge C/electron *)
planck=6.626 10^-34 10^-9 (* Planck's constant, Joule ns *)

(* THERMAL EFFECTS PARAMETERS *)
b=.00025 (* gain spectral shift for temp in microns/K .0003*)
Ton = 0 (* set Ton to 1 to include temperature effects, *)
(* set to 0 to ignore effects *)
T1=400 (* Temp. inc.in active layer from Ith to Ip CW, ns *)
T2=1500 (* Thermal time constant of active layer in ns*)
K1=.295 (* Temp. increase in active layer for time constant T1, deg.K *)
K2=.41 (* Temp. increase in active layer for time constant T2, deg. K *)
TO=125 (* TO is the scale factor (in deg. K) for the shift in *)
(* current threshold for change in temperature *)
jon=0 (* set jon to 1 to include shift in current threshold due to temp..*)
(* set to 0 to ignore *)

(* SPECTRAL PARAMETERS *)

Bandtype=1 (* which way to define bandwidth, 1 = lorentzian, 2 = modified Lorentzian *)
B0=.025 (* gain spectral half width for Lorentzian in microns *)
B1=.026 (* gain spectral halfwidth for modified Lorentzian, in microns*)
B2=.014 (* gain spectral halfwidth for modified Lorentzian, second parameter *)
lambdap=0.812 (* wavelength at peak of distribution *)
v=.000 (* gain spectral peak offset, in microns*)
(* to make symmetric, make v=0.*)
vdeltaLc/2 sets center of gain curve between 2 modes*)
M=9 (* number of modes = 2M+1, maximum is 11*)

xu=.01064 (* gain spectral shift for carrier density (.1064), microns *)
u=0 (* set u=0 to ignore spectral shift for carrier density *)

(* n = electron density, t = time, ns *)
(* G0, G1, G2, etc. are the gain factors for the individual modes *)
(* s0, s1, s2 etc. are the photon densities of the individual modes *)

EnergyJ = planck c/lambdap (* energy per photon, J/photon *)

-19
2.44803 10

```

```

nsteps=Round[(timeend-timestart)/.35] (* approx. no. of steps used by simulation*)
57
deltaLc=lambdap^2/(2 ng L) (*mode separation, in microns*)

0.000312189
DT = Ton*(K1(1-Exp[-t/T1])+K2(1-Exp[-t/T2])) (*temp. change as a fcn of time during pulse*)
0
DT2 = jon*(K1(1-Exp[-t/T1])+K2(1-Exp[-t/T2]))
(*threshold shift-temperature change as a function of time during the pulse*)
gamma=#[(K eta*lambdap^4)/(4 Pi^2 ng nr^2 dthickness width L B0)] (* spontaneous emission factor *)
0.000114056
ntrans=trans Exp[DT2/TO]
29
-----
2000000000000000000
beta2=beta2p Exp[-DT2/TO]
13
4.4 10
A=((beta2 ee dthickness)/tsp) (c/ng) (*stimulated emission factor,microns^3/ns*)
0.0084
r=(refl refl2)^.5 (*reflectivity of the mirrors *)
0.533854
alpha=#[(alpha+(1/L) Log[1/r])] (* loss coefficient *)
0.00499211

tp=ng/(c alpha) (* photon lifetime, ns *)
0.00235038
tp2=ng/(c ((1/L) Log[1/r])) (*average time photons spend in cavity*)
0.00560837
j2=current/(L width) (* current density,C/ns/micron^2 *)

-14
1.11111 10
j=(j2/(dthickness ee))*A*tsp*tp (*normalized electron density,electrons/(micron^3 ns) *)
97.9323
no=#[(ntrans/ee*tsp/dthickness) A tp]
(*transparency current density for dominant mode, with temperature effects *)
M01=10^9 width/.97 (L trans)
0.0269072
M02=10^9 width/.97 (L alpha/(eta beta2))
0.027179
M03=10^9 width/.97 (Log[1/r]/(eta beta2))
0.0196074
Ith=M01+M02+M03 (*calculated threshold current, amps *)
0.0736936
UU= u(1-n/no) (* shift in gain peak due to carrier density change *)
0
Lvp[x_] := UU-h DT +x deltaLc +v (* difference between mode wavelength and gain peak *)
W[x_] :=If[Bandtype<1.5,1/(1+(Lvp[x]/B0)^2),1/(1+(Lvp[x]/B1)^2+(Lvp[x]/B2)^4)]
(* denominator of line shape factor *)
D0=#[0]
1.

G0=D0 (n-no)
1. (-12.7802 + n)

```

```

D1=If[M>0,W[1],0]

0.999844
G1=If[M>0,D1 (n-no),0]
0.999844 (-12.7802 + n)
D2=If[M>0,W[-1],0]
0.999844
G2=If[M>0,D2 (n-no),0]
0.999844 (-12.7802 + n)

D3=If[M>1,W[2],0]
0.999377
G3=If[M>1,D3 (n-no),0]
0.999377 (-12.7802 + n)
D4=If[M>1,W[-2],0]
0.999377
G4=If[M>1,D4 (n-no),0]
0.999377 (-12.7802 + n)

D5=If[M>2,W[3],0]
0.998599
G5=If[M>2,D5 (n-no),0]
0.998599 (-12.7802 + n)
D6=If[M>2,W[-3],0]
0.998599
G6=If[M>2,D6 (n-no),0]
0.998599 (-12.7802 + n)
D7=If[M>3,W[4],0]
0.997511
G7=If[M>3,D7 (n-no),0]
0.997511 (-12.7802 + n)
D8=If[M>3,W[-4],0]
0.997511
G8=If[M>3,D8 (n-no),0]
0.997511 (-12.7802 + n)
D9=If[M>4,W[5],0]
0.996117
G9=If[M>4,D9 (n-no),0]
0.996117 (-12.7802 + n)
D10=If[M>4,W[-5],0]
0.996117
G10=If[M>4,D10 (n-no),0]
0.996117 (-12.7802 + n)
D11=If[M>5,W[6],0]
0.994418
G11=If[M>5,D11 (n-no),0]
0.994418 (-12.7802 + n)
D12=If[M>5,W[-6],0]
0.994418
G12=If[M>5,D12 (n-no),0]
0.994418 (-12.7802 + n)

```

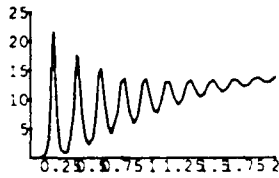
```

D13=If[M>6,W[7],0]
0.992417
G13=If[M>6,D13 (n-no),0]
0.992417 (-12.7802 + n)
D14=If[M>6,W[-7],0]
0.992417
G14=If[M>6,D14 (n-no),0]
0.992417 (-12.7802 + n)
D15=If[M>7,W[8],0]
0.990118
G15=If[M>7,D15 (n-no),0]
0.990118 (-12.7802 + n)
D16=If[M>7,W[-8],0]
0.990118
G16=If[M>7,D16 (n-no),0]
0.990118 (-12.7802 + n)
D17=If[M>8,W[9],0]
0.987526
G17=If[M>8,D17 (n-no),0]
0.987526 (-12.7802 + n)
D18=If[M>8,W[-9],0]
0.987526
G18=If[M>8,D18 (n-no),0]
0.987526 (-12.7802 + n)
D19=If[M>9,W[10],0]
0
G19=If[M>9, D19 (n-no),0]
0
D20=If[M>9,W[-10],0]
0
G20=If[M>9, D20 (n-no),0]
0
D21=If[M>10,W[11],0]
0
G21=If[M>10,D21 (n-no),0]
0
D22=If[M>10,W[-11],0]
0
G22=If[M>10,D22 (n-no),0]
0
gains=1+eps (a0+a1+a2+a3+a4+a5+a6+a7+a8+a9+a10+a11+r1+r2+r3+r4+r5+r6+r7+r8+r9+r10+r11) / (tsp A)
1
nt=A tp (1/(A tp)+no/(A tp))
13.7802
neo=30
30

```

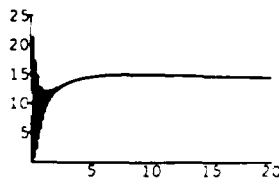


```
fn=ListPlot[Table[ {f[[k,1]], f[[k,3]]*((L width dthickness/eta Energy) (1/tp2 10^9) 10^3/(tsp Axx))},
{k,1,Length[f]}],PlotJoined -> True,PlotRange->{{timestart,timeend}/noticks},{0,estpower/2} ]
```



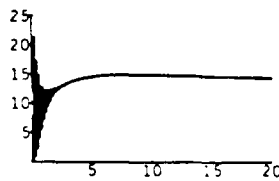
-Graphics-

```
fn=ListPlot[Table[ {f[[k,1]], f[[k,4]]*((L width dthickness/eta Energy) (1/tp2 10^9) 10^3/(tsp Axx))},
{k,1,Length[f]}],
PlotJoined -> True,PlotRange->{{timestart,timeend},{0,estpower/2}},
Ticks ->{Range[timestart,timeend,(timeend-timestart)/noticks],Range[0,estpower/2,estpower/2/noticks2]}
```



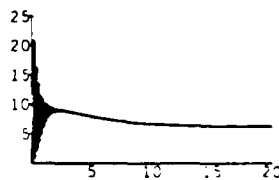
-Graphics-

```
fn2=ListPlot[Table[ {f[[k,1]], f[[k,5]]*((L width dthickness/eta Energy) (1/tp2 10^9) 10^3/(tsp Axx))},
{k,1,Length[f]}],
PlotJoined -> True,PlotRange->{{timestart,timeend},{0,estpower/2}},
Ticks ->{Range[timestart,timeend,(timeend-timestart)/noticks],Range[0,estpower/2,estpower/2/noticks2]}
```



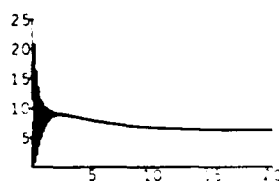
-Graphics-

```
fn=ListPlot[Table[ {f[[k,1]], f[[k,6]]*((L width dthickness/eta Energy) (1/tp2 10^9) 10^3/(tsp Axx))},
{k,1,Length[f]}],
PlotJoined -> True,PlotRange->{{timestart,timeend},{0,estpower/2}},
Ticks ->{Range[timestart,timeend,(timeend-timestart)/noticks],Range[0,estpower/2,estpower/2/noticks2]}
```



-Graphics-

```
fn=ListPlot[Table[ {f[[k,1]], f[[k,7]]*((L width dthickness/eta Energy) (1/tp2 10^9) 10^3/(tsp Axx))},
{k,1,Length[f]}],
PlotJoined -> True,PlotRange->{{timestart,timeend},{0,estpower/2}},
Ticks ->{Range[timestart,timeend,(timeend-timestart)/noticks],Range[0,estpower/2,estpower/2/noticks2]}
```

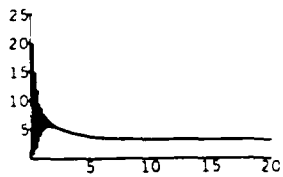


-Graphics-

```

fn=ListPlot[Table[ {f[[k,1]], f[[k,0]]*((L width dthickness/eta Energy) (1/tp2 10^9) 10^3/(tsp Axx))},
  {k,1,Length[f]}],
  PlotJoined -> True,PlotRange->{{timestart,timeend},{0,estpower/2}},
  Ticks ->{Range[timestart,timeend,(timeend-timestart)/noticks],Range[0,estpower/2,estpower/2/noticks2]}]

```

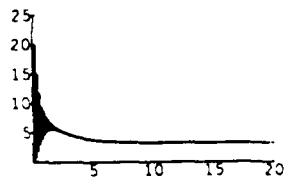


-Graphics-

```

fn=ListPlot[Table[ {f[[k,1]], f[[k,0]]*((L width dthickness/eta Energy) (1/tp2 10^9) 10^3/(tsp Axx))},
  {k,1,Length[f]}],
  PlotJoined -> True,PlotRange->{{timestart,timeend},{0,estpower/2}},
  Ticks ->{Range[timestart,timeend,(timeend-timestart)/noticks],Range[0,estpower/2,estpower/2/noticks2]}]

```



-Graphics-